NOTE TO USERS

F_2-LASER MICROFABRICATION OF LAB-ON-A-CHIP STRUCTURES

by

Stephen PaulChi Ho

A thesis submitted in conformity with the requirements
for the degree of Master of Applied Science
Graduate Department of Electrical and Computer Engineering
University of Toronto

Your file Votre référence
ISBN: 0-494-02206-X
Our file Notre référence
ISBN: 0-494-02206-X

Abstract

F_2-laser microfabrication of lab-on-a-chip structures

Stephen PaulChi Ho

Master of Applied Science

Graduate Department of Electrical and Computer Engineering

University of Toronto

2005

For cellular biology, the idea of incorporating the capabilities of sample preparation, transport, reaction and analysis on a single chip has recently been revisited due to the development of a new generation of microfabrication tools. The rapid growth of interest in the microfabrication of lab-on-a-chip devices is fueled both by academia and industry because of the potential impact in fields such as biomedical, chemistry and biophysics. Direct photoablation with lasers has advantages of rapid prototyping, custom production and design flexibility.

In this thesis, the microfabrication of lab-on-a-chip structures for biophotonics application using F_2 laser are presented. Fabrication of buried and surface waveguides provides a means of probing bio-materials. Investigation of F_2-laser welding allows potential fusing for enclosure glass biochips. A combination of laser micromachining and refractive index profiling enable single-step integration of optical waveguides with microfluidic functions for optical sensing of microspheres which lays the groundwork for microfabrication of biochips.

Acknowledgements

I would like to thank my supervisors, Professor Peter Herman and Stewart Aitchison, for their guidance, inspiration, and encouragement. Thanks to our collaborators, Professor Koji Sugioka, Dr. Cheng Ya and Katsumi Midorikawa, whose ideas and advices had led to a successful Foturan project. Thanks also goes to Alison Cleary for the collaboration on the FHD work. I would also like to thank the photonics group members: Andrew Yick (past group member) for his valuable viewpoints, Shane Eaton and Chris Valdivia for their expert advice in optical circuits, Sonia Garcia-Blanco for her useful inputs, Eddy Chan, Mi Li Ng, Dr. YuanKun Lin, Haibin Zhang, James Dou, Matthew Wronski, and Amir Nejadmalayeri. A special thanks to Dr. JianZhao Li for his generous help in operation of the F_2 laser and countless suggestions which were of great value for my project. Last but not least, I would like to thank all my family members and friends who had given me constant support and love for accomplishing my thesis.

Contents

List of Tables

List of Figures

Chapter 1

Introduction

The development of the lab-on-a-chip devices is a field of rapid growth. The idea of incorporating the capabilities of sample preparation, transport, reaction, and analysis on a single chip was first demonstrated in the 1970s [1]. A complete gas chromatography system was integrated on a 2" silicon wafer by Terry et al [1]. However, this work went unnoticed for almost twenty years until the concept of micro-total-analysis-system (μ-TAS) once again emerged in 1990 [2]. This led to an exponential growth in this field both in academic and now in commercial businesses.

A biophotonic lab-on-a-chip combines micro-channel networks with optical functionalities. Depending on the application, various components including micro-optics, Bragg grating filters, optical circuits, and micro-channel networks can be integrated onto a single chip with countless configurations. These building blocks are readily fabricated individually with direct laser technique. However, the sequential integration of these components with direct laser microfabrication has yet to be demonstrated with a single laser source. The combination of laser induced refractive index change with the micromachining capability allows an all-in-one fabrication technique for efficient and cost-effective rapid prototyping of biophotonics lab-on-a-chips.

Current fabrication techniques for lab-on-a-chip devices are based on advances in the

microelectronic industries. The most common direct fabrication technique for microfluidic channels is based on photolithography and wet etching [3–6]. Photolithography combined with reactive ion etching is also used to fabricate planar optical waveguides and micro-channels [7, 8] with a sub-micron resolution. However, photolithography based techniques require a multi-step process which is not suitable for a low volume, rapid prototyping research environment. It is time consuming and expensive to operate because a slight change in design requires a newly fabricated mask for exposure. Further, chemicals involved can be hazardous. However, photolithography is a well developed technique for the mass production of an optimized design without continuous adjustments in design. Other techniques are developed for lab-on-a-chip fabrication including stereolithography [9, 10], and laser photoablation [11].

Direct laser photoablation and refractive index modification have the advantages of rapid prototyping and low volume production for custom designs. They provide a flexible method of writing complex, smooth-walled micro-channel networks and buried refractive index structures with a few processing steps. Depending on the desired patterns and features, an amplitude mask with appropriate aperture(s) is used. A computer controlled laser exposure allows different structures to form on the surface, or within the target sample. A post laser exposure step may be performed to remove redeposited debris on the sample surface. The design can be programmed into the computer which controls the sample mounted motion stage. This offers a simple solution for design adjustments. The fabrication time ranges from minutes for simple designs to hours for complicated designs. Hence, this approach can incorporate various designs on a single sample sequentially and more importantly, it allows the integration of optical waveguides with micro-channels on a single glass chip.

Common bonding and sealing techniques for microfluidic devices including lamination and gluing have the disadvantage of potentially blocking very small channels. The use of adhesives in the bonding technique has a potential hazard of producing toxic fumes.

Polydimethylsiloxane (PDMS) can be used to seal microfluidic channels because it is flexible and can conform to minor imperfections. However, this seal can only withstand low pressure of <5 psi [12]. Laser welding provides another means of bonding and sealing these glass devices with the merits of precise welding and alleviating the problem of conventional bonding methods. The substrates to be bonded are pressed together allowing efficient heat conduction between the materials. A laser beam penetrates through the first substrate and gets absorbed by the second substrate, and fusing occurs at the contact points. The welding spots can be shaped by the mask aperture and controlled by the laser energy, repetition rate, and pulse duration. Laser transmission welding is a clean and efficient approach for glasses.

The combination of photosensitivity, laser micromachining and welding offer the prospect for rapidly prototyping lab-on-a-chip components in a range of materials. This is the aim of this thesis: Monolithic integration of optical components, namely waveguides, into a lab-on-a-chip structure with microfluidic channels. The significance of the incorporation of optical abilities for probing and manipulation of the sample content in the lab-on-a-chip is that it opens up a wide range of systems possibilities and is the logical step forward. The lab-on-a-chip provides the platform for sample preparation, transport and reaction. In addition, the optical circuit adds to it the capability of analyzing the sample content.

1.1 Thesis Objectives

The main objective of this thesis is to demonstrate the monolithic integration of optical components with microfluidic structures in glasses with the F_2-laser microprocessing system. The research presents the microfabrication and investigation of the following areas:

1. Welding of a fused silica slip to a standard glass optical fiber to demonstrate a po-

tential method of enclosing glass lab-on-a-chips with optically transparent glasses.

2. Fabrication of waveguides and Y-branches in flame hydrolysis deposited (FHD) Ge-doped silica using direct laser exposure of patterned NiCr contact mask for possible lab-on-a-chip platform.

3. Direct laser writing of shallow buried optical waveguides with depths from 10 μm to 25 μm from the bulk fused silica surface for later integration with microfluidic channels, and optical probing of particles and bio-materials.

4. Optimization of laser ablation for fabrication of microfluidic channels to allow fluid transport and optical analysis of bio-materials inside micro-channels.

5. Integration of optical waveguides and microfluidic channels for optical probing and detection of particles and bio-materials.

1.2 Chapter-by-Chapter Outline

The following outline presents a brief description and overview of each chapter:

- Chapter 2 "Background - Biophotonic Lab-on-a-Chip": This chapter reviews the current state-of-the-art technology used in the microfabrication of biophotonic lab-on-a-chip. Advanced laser processing provides a means for laser ablation and welding. The discovery of photosensitivity in glass and the current photonics technology in optical circuit and waveguide fabrication are presented. Various biochips and biophotonic lab-on-a-chip microfabrication techniques, designs and applications are described to provide the breadth of these devices.

- Chapter 3 "Experimental Setups and Designs": This chapter presents a thorough description of the experimental setup and design parameters. The specification of the F_2-laser system used throughout this research is presented. The laser processing

parameters and setups for laser welding, waveguide and optical circuit writing, and microfluidic channel ablation are described in detail. Further, the setup and procedures for characterization of optical circuits and the integrated device are covered in-depth.

- Chapter 4 "Results and Discussions - Laser Processes": This chapter presents the results and discussions for each of the biophotonic lab-on-a-chip components, namely, laser welding of glasses, F_2-laser fabrication of optical circuits in FHD Ge-doped silica and buried waveguide in bulk fused silica. These materials provide an ideal platform for integrating waveguides with microfluidic structures. The processing windows and characterization results are presented followed by a discussion of the main findings.

- Chapter 5 "F_2-Laser Microfabricated Biophotonic Device": This chapter presents the results and discussions for the integrated device with buried waveguide integrated with microfluidic channel. The insertion loss is addressed together with the detection sensitivity tested with polystyrene microsphere.

- Chapter 6 "Significance of this Work": This chapter presents the significance of this research which encompasses the work in laser welding, Ge-doped FHD silica optical circuits fabrication and monolithic integration of waveguides and micro-channels. This work provides insight into the development of biophotonic lab-on-a-chip design and application.

- Chapter 7 "Conclusions": This chapter presents a summary of this research work which concludes this thesis.

Chapter 2

Background – Biophotonic Lab-on-a-Chip

Photonics deals broadly with the interactions and applications of photons. By replacing electrons with photons, we have seen a dramatic improvement in the capacity and speed of data transmission, processing and storage. These advances in photonics have also led to the development of applications in biology, medicine, and imaging which triggered the development of biophotonics.

Biophotonics is a field which uses the established technologies in photonics to aid the analysis of biological materials. Biophotonics is advancing rapidly as new photonics technologies are developed. However, biology is also placing new demands on photonics since the biomedical field requires new photonic developments to accommodate the growth of biotechnology.

The interaction of light with biological samples is present in our everyday lives from basic life functions such as photosynthesis to advance laboratory diagnostics and therapy for healthcare such as microscopy and photodynamic therapy. Current fabrication techniques are borrowed from the semiconductor industries. Photolithography, stereolithography and wet etching provide one means to shrink a full size laboratory into a

microchip sized device. Laser micromachining is an alternate approach for direct microfabrication that readily provides submicron features in a wide variety of materials. It is able to incorporate photonic capabilities including optical circuits and Bragg gratings with microfluidic structures. Hence, a biophotonic lab-on-a-chip device combines the light interaction and diagnostic of bio-materials plus the advantage of bringing a chip sized laboratory into a functional device.

Direct laser processing offers many advantages over conventional photolithographic or mechanical techniques. It is a single-step process as opposed to photolithography which involves multiple steps and hazardous chemicals. Laser micromachining provides a non-contact processing means to minimize tool wear and the risk of mechanical damage. Moreover, complex geometries and depth profiles can be implemented by controlling the wavelength, power, laser repetition rate and motion of the focal spot. This allows for high flexibility and rapid prototyping.

The literature being discussed is mostly concentrated on microprocessing of glass materials. The main focus is on amorphous fused silica glass which has the advantages of high optical transparency, durability, thermal stability, high purity and the ability to be doped with other materials such as germanium and boron. Moreover, glass has been used extensively in the optoelectronic industries [13]. It has high transmission from UV to infrared and has low nonlinearity and dispersion. These favorable physical and optical properties combine to create a suitable substrate for fabrication of optical circuits together with lab-on-a-chip structures.

In this chapter, a review of the available laser processing and fabrication techniques, applied to lab-on-a-chip devices, will be presented.

2.1 Advanced Laser Processing

Since the demonstration of the ruby laser in 1960 by Theodore Maiman [14], a new energy source has emerged for the microprocessing of materials. With this novel source, a collimated beam of light can be focused to a small spot size producing a high power density which allows efficient material interactions. This opens up new opportunities in material processing and has also fueled the academic and commercial development laser processing. Direct laser ablation, welding and chemical modification are only a few applications being explored and employed for a wide range of materials including glasses.

2.1.1 Laser Ablation

Direct laser ablation offers advantages over other fabrication methods, namely, small heat affected zones, precise control over machining depth, and rapid throughput. Moreover, it allows contact free micromachining with a high degree of automation and scalability.

Photoablation of glass, especially fused silica, is challenging for most lasers because of the weak light interactions inherent in such transparent substrates. Fused silica, with its high transparency from the visible to near-infrared wavelength, is used widely in the telecommunication and optics community. The vacuum ultraviolet (VUV) F_2 laser emits at a wavelength of 157 nm, that corresponds to a photon energy of 7.9eV. The F_2 laser pulse duration is 15 ns. Herman et al. have demonstrated ablation of polymers, quartz, semiconductors [15] and fused silica [16] using this laser system.

Although fused silica has a large bandgap of 9.3 eV equivalent to a wavelength of 133 nm [17], a single-photon ablation process is possible at 157 nm due to native defects near the band edge. These defects lower the absorption edge of fused silica to $\sim$170 nm or a photon energy of 7.3 eV [18]. Also in the ablation study of fused silica, the single-pulse etch rate follows a logarithmic fluence dependence with an absorption coefficient of 10 cm^{-1} at 157 nm [16]. Therefore, fused silica is able to absorb the F_2 laser radiation

causing effective ablation.

A comparison of VUV laser ablation using 193 nm and 157 nm was carried out by Herman et al [17]. Using 193 nm laser radiation, a transparent layer of Ge-doped fused silica and fused silica on an absorbing silicon was damaged by ejection of the glass layer due to laser heating at the glass-silicon interface. On the other hand, using 157 nm laser radiation provided a smooth, uniform excision with excellent control of ablation depth [17]. The ablation threshold of fused silica is 1.1 J/cm^2 while the threshold for 8% Ge-doped silica is 0.38 J/cm_2 a value 70% less than fused silica [17].

Another technique used in the photoablation of fused silica involve excited-state absorption (ESA) by combining KrF and F_2 laser beams. The F_2 laser radiation is absorbed by the fused silica and electrons can be excited to defect levels. The presence of these excited states increases the absorption of the KrF excimer laser such that the photon energy of 5.0 eV leads to Si-O bond scission to provide clean ablation [18].

The quality of laser machined structures varies according to laser wavelength, repetition rate, power density, and material properties. Korner et al. introduce four principal classes of fundamental processes for the long pulse duration (in ns regime) ablation [19]. These are spallation, near threshold evaporation, above threshold stationary evaporation, and stationary melt displacement and ejection. Different mechanisms dominate depending on the material and the processing parameters chosen. The geometry of the heat affected zone (HAZ), mechanical affected zone (MAZ), and chemical affected zone (CAZ) is determined by these fundamental processes. With ns laser pulses, the ablation mechanism is mainly due to evaporation, melt ejection or spallation.

The four classes of ablation mechanisms described by Korner et al. are listed below [19]:

1. Type A: *Ablation by spalling.* This mechanism occurs when weakly absorbing, brittle materials are ablated by laser energy that is much smaller than the binding energy or the latent heat of melting. Whole pieces of material can be ejected due

to mechanical stresses accumulated inside. Formation of cracks is also observed.

2. Type B: *Ablation by near threshold evaporation.* This mechanism occurs because a large portion of the laser energy is deposited as heat in the material and only the end of the pulse is used for ablation. The topography generated from the initial pulse alters the absorption of subsequent pulses which enhances the beam and material inhomogeneities. The ablation begins when the surface temperature (T) reaches the evaporation temperature given by the following one-dimensional heat conduction equation (Equation 2.1):

$$T = \frac{P\sqrt{4D_T t}}{f\sqrt{\pi}} \tag{2.1}$$

where P is the power density, D_T is the thermal diffusivity, t is the time and f is the thermal conductivity.

The thermal penetration depth is given by (Equation 2.2):

$$d_T = \sqrt{4D_T \tau} \tag{2.2}$$

where τ is the pulse duration (FWHM).

3. Type C: *Ablation by above threshold stationary evaporation.* This mechanism occurs when the pulse fluence is enough for the surface to reach the evaporation temperature near the beginning of the laser pulse. However, the ablation and vapor pressure are insufficient to eject molten material. A narrow profile forms at the bottom of a deep ablation due to multiple-reflections.

4. Type D: *Ablation by far above threshold stationary melt displacement and ejection.* This mechanism occurs when the fluence is high enough to eject molten material due to the ablation and plasma pressure. Large aspect ratio walls can be ablated with the melts redeposited to create smooth walls.

Figure 2.1 illustrates the ablation profiles due to the four different types of ablation mechanisms.

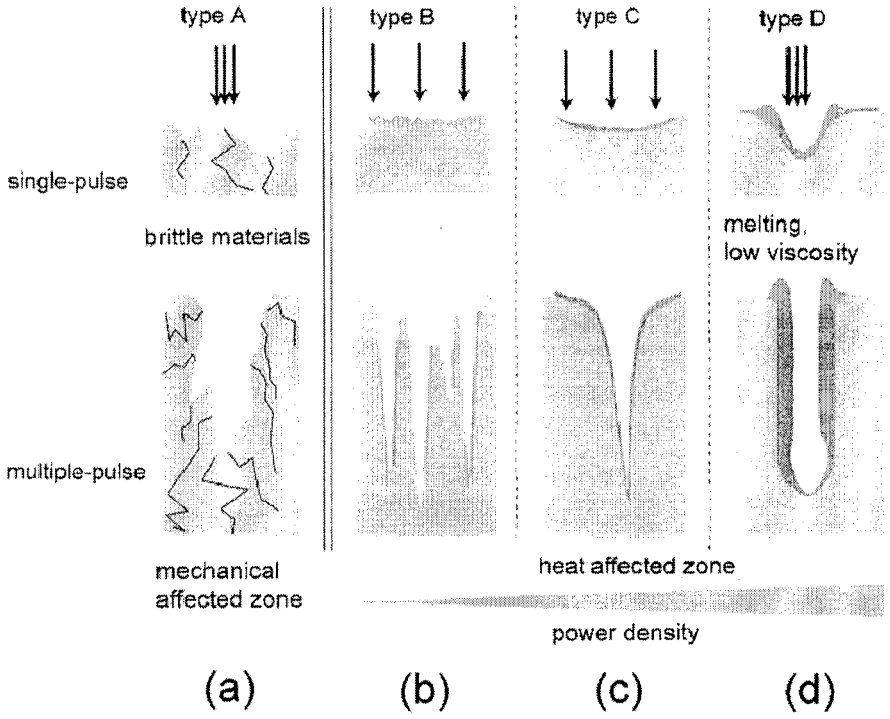

Figure 2.1: The four different classification of the fundamental ablation mechanisms and the resultant ablated profiles due to single or multiple-pulse: (a) microcracks formation in brittle materials, (b) inhomogeneous profile, (c) narrow V-groove profile, and (d) large aspect ratio wall. The power density increases from type B to type D (left to right). The picture is reproduced from Korner et al. [19]

As the power density increases, a type B ablation mechanism will progress to a type C

and eventually to a type D process. Since type A ablation is determined by the brittleness of the material, co-occurrence of A+B, A+C and A+D is possible. Hence, the ablation phenomenon not only depends on the material properties, it also depends on the power density of the laser beam. For fused silica, type A ablation mechanism can play a role. However, the dominating mechanism is imposed by the power density which progresses from type B to D with increasing fluence.

2.1.2 Laser Welding

Laser welding is an important commercial application in metallurgy. However, research and development on the welding of glass and silicon are not as well developed. The development of laser welding of glasses offers several benefits. Firstly, there is no physical contact between the material and the heating source resulting in clean product. Secondly, laser welding produces no toxic fumes in comparison to other bonding techniques involving adhesives and bonding agents. It also offers speed, precision, design flexibility, and controllability by regulating the laser energy, wavelength, and motion of the focal spot.

The most common lasers for welding glasses are Nd:YAG and CO_2 lasers. These lasers are well developed and have high output powers of 100 W to over 1 kW for Nd:YAG and 0.5 to over 25 kW for CO_2 lasers [20–25]. Further, diode lasers have also been used widely to fuse glass to silicon [26].

Bonding of glasses and non-metallic materials traditionally involves coating a layer of bonding material onto the substrate and subsequent melting of this layer. Recent methods employ laser heating. The absorbent is coated on the welding area of the glass surface and hence YAG laser radiation is absorbed only at the coated area [20]. This technique allows the bonding of glasses to other materials in a pre-defined area. However, it requires multiple steps and the absorbent coating step is inconvenient and inefficient.

Glass-silicon bonding is another application for laser welding because of the vast array

of optoelectronic components requiring attachment of micro-sized optical components. The conventional methods include the use of adhesives [27, 28] and anodic bonding [29–31]. Direct laser bonding is a promising alternative. The use of YAG lasers is being studied for laser welding of glass to silicon by using the principle of transmission welding in which the laser beam is transmitted through the glass substrate and absorbed by the silicon [21–23]. A speed of 50 to 500 mm/min can be achieved. Moreover, the introduction of high power diode lasers (less than 50 W) has enabled efficient and cost effective glass-silicon laser welding [26].

Glass-to-glass welding has also been demonstrated using the transmission welding method. Phitzer et al. pioneered the use of CO_2 laser for welding of fused silica glass [24]. Further work on CO_2 laser welding of fused silica glass was done by Deminet in which a thin fused silica cane was used to initiate the welding process and the laser melted glass brought the surfaces together by surface tension [25]. Joeckle et al. demonstrated HF chemical laser welding of glass. With the wavelength range of HF chemical laser, several laser lines are strongly absorbed by glass which allows bulk heating [32]. A speed of 20 cm/min was demonstrated. However, the bulk heating effect caused high thermal stresses which produced fractures.

Laser through-transmission welding is a technique in which laser energy is transmitted through one of the parts to be welded to cause subsequent melting and diffusion of material in the interfacial or weld-plane zone [33]. The second material absorbs the light, producing intense local heating and softening/melting at the interface between the materials. Ideally, one material will be completely transparent to the light and the other will have high absorption. Pressure must be applied to force the parts together and restrict the expansion of the heated materials. The close contact will allow transfer of heat from the more absorbing material to the non-absorbing material for more uniform heating.

2.2 Photonics Technology

The first observation of photosensitivity in a Ge-doped silica-core optical fiber induced by laser light was reported by Hill et al. in 1978 [34]. A 488 nm light was employed to imprint a permanent periodic refractive index change in the optical fiber with a weak index modulation on the order of 10^{-6}. After almost a decade, Meltz et al. used a two-beam interference pattern at a wavelength of 244 nm to produce Bragg gratings by exposing the core from the side [35]. This new technique combined with a wavelength which lies in the oxygen-vacancy defect band of germania provided an index modulation of $3x10^{-5}$. More work on Bragg gratings has been done by various groups using 193 nm ArF laser [36, 37], 248 nm KrF laser [36] and more recently by 157 nm F_2 laser [38]. The next generation photosensitivity applications are focused on buried and planar light circuits.

2.2.1 Photosensitivity

The photoinduced refractive index change mechanism is currently not fully understood. There are several models that have been proposed to explain these photoinduced refractive index changes including the color center model and the compaction model [39]. However, not one of these can be used alone to explain the refractive index change in glass.

Hand and Russel proposed the color center model in which the UV light produces new electronic transitions of defects, or color centers, in the irradiated glass [40]. In this model, the refractive index is determined by the electronic absorption spectra from the defects and it relates to the number density and the orientation of the defects. The photosensitivity arises from the fact that there are localized electronic excitations associated with the defects. Through the Kramers-Kronig relationship (Equation 2.3), the photoinduced changes in the absorption spectrum give rise to the refractive index change

[41]:

$$\epsilon_r(\lambda) = 1 + \int \frac{\epsilon_i(\lambda)}{\lambda' - \lambda} d\lambda' \tag{2.3}$$

which relates the real and imaginary parts of the dielectric constant $\epsilon = (\mathrm{n}+\iota\ \kappa)^2$ where n is the refractive index and κ is the absorption index.

Williams et al. performed measurements of UV irradiated absorption spectrum of germanosilicate fiber between 200 nm and 350 nm showing an intense absorption centered at 242 nm. Evidence of color center model was shown by bleaching of the 240 nm band under UV irradiation which was consistent with the Kramers-Kronig relationship [42]. Dong et al. further demonstrated the photoinduced absorption changes between 165 nm and 300 nm showing evidence for the color center model of photosensitivity in UV written fiber gratings [43].

The compaction model is a densification of the glass material induced by laser irradiation. This relative density change, $\Delta\rho/\rho$, results in a refractive index change. It has been found that the densification process can be described theoretically [44–47]. For two photon absorption processes, such as that produced by 193 nm or 248 nm laser irradiation, the power-law fit is as follows (Equation 2.4):

$$\frac{\triangle\rho}{\rho} = a(\frac{F^2 N}{\tau})^b \tag{2.4}$$

where F is the fluence, N is the number of pulses, τ is the integral squared pulse duration of the laser, a is the photosensitivity rate and b is the order of process.

For 157 nm irradiation, which is a single photon absorption process, the power-law fit becomes (Equation 2.5):

$$\frac{\triangle\rho}{\rho} = a(FN)^b \tag{2.5}$$

where a and b have values of 10^{-5} to 10^{-4} and 0.5 to 0.7, respectively, for fused silica glasses.

Densification of fused silica inducing a refractive index change with UV irradiation has been demonstrated [46, 48, 49]. Piao et al. explained that the densification effect is due to the excess energy stored in the bridging Si-O-Si bonds in fused silica which acts as the driving force for bridging bond relaxation. This results in a smaller average bridging bond angle such that a smaller Si-Si distance provides the densification effect [48]. Friebele and Higby suggested the cleavage of ring structures induced from UV irradiation with subsequent formation of closely packed smaller ring structures lead to densificiation [50]. Further study is required to delineate the basic response mechanism.

Ultrafast laser offers an alternative mean for direct refractive modification in glasses. Direct writing of optical waveguides in Ge-doped silica using an ultrafast laser [51] and fused silica [52] extended the laser direct-write approach to allow the full 3-D writing of photonic structures within the bulk glass. Multiphoton ionization, electron avalanche [53, 54], and micro-explosions [55] are the fundamental interactions which lead to refractive index change through compaction and/or color centers. Further, the ultrashort pulses are subjected to a nonlinear effect in glasses which produces sub-spotsize features and prevents the heat affect zone due to the short pulse.

2.2.2 Optical Circuits and Waveguides

This section reviews laser writing of optical circuits and waveguides in silica glass. Such light guiding structures can be extended to lab-on-a-chip integration to enhance the vast breadth of applications these biochip devices presently offer.

Several methods have been established for the commercial fabrication of optical circuits. Waveguides with Bragg grating filters are fabricated in silicon-on-insulator with electron beam lithography and plasma-assisted reactive ion etching (RIE) [56]. Other techniques include combinations of lithography, molecular beam epitaxy (MBE), chemi-

cal vapor deposition (VCD), chemical etching [57,58], electron beam densification [59], and ion-exchange [60]. These fabrication techniques deliver high quality and high volume photonic devices suitable for industrial applications.

A more flexible method that does away with multi-step lithography is that of refractive index modification by direct laser writing of photonic circuits. Such direct write methods are better suited to research and development efforts, and rapid prototyping. Direct writing of waveguides [61] and Y-branch power splitters [62] in Ge-doped silica glass have been demonstrated by using a 244 nm argon-ion laser. Here, a two photon absorption process underlies the direct writing of buried waveguide, yielding a refractive index change of $5x10^{-5}$ in pure fused silica glass [63]. Herman and coworkers have written buried waveguide structures with 157 nm radiation from a F_2 laser, in fused silica glass, providing a refractive index increase of 10^{-3} [49]. This is effectively a single photon process because of the high energy photon and produces a positive index change which requires net fluences of 10 to 40 kJ/cm^2 to generate an index increase of 10^{-4} to 10^{-3} [64]. These red confining waveguides were later found to guide infrared light [65]. The F_2 laser was also used to induce planar waveguides in germanosilica glass with a refractive index of more than $5x10^{-3}$ [66]. The photosensitive response was demonstrated to be more than 15 times stronger than KrF laser operating at 248 nm and more than 2 times stronger than produced by a 193 nm ArF laser.

Microfabrication of optical circuits with UV lasers has proven to be reproducible and yield high quality components. The F_2-laser direct write method provides a positive refractive index change of up to 10^{-3} that is attractive for producing waveguide and other photonic components in fused silica and germanosilica glass.

2.3 Biochips

Biochip is a general term describing arrays of microfluidics, sensors, and chemical synthesis on-chip. Biochips are also related to μTAS, which is also called a lab-on-a-chip. The concept of miniaturization of on a single analytical devices was first demonstrated more than 25 years ago by Terry et al. [1] who fabricated a miniaturized chromatographic analyzer on a silicon wafer. The analyzer was able to separate a compound mixture in seconds. There was no immediate response from the scientific community and this work went unnoticed. The silicon effort was principally directed toward the fabrication of micropumps [67–70] and microvalves [69–72], though diagnostic and analyzing components were only a minute part of the objectives.

In 1990, Manz et al. presented the novel device of a miniature open-tubular liquid chromatograph on a 5 mm x 5 mm silicon chip [73]. They also proposed the concept of μTAS in which sample pretreatment, separation and detection were all incorporated [2]. The reduction in size not only enhanced the performance of measurements, it also required less consumption of reagent and analyte. The promise of integrating different components within a single miniature platform allows for a reduction in time and cost while increasing the number of device functions. These integrated device offered sample preparation, transport, reaction, analysis, diagnostics and measurement to define a powerful tool on a single microchip device.

2.3.1 Biochips Fabrication Techniques

There are numerous techniques applied in the microfabrication of biochips. Many methods are borrowed from the well established semiconductor industry. Photolithography is among one of the most common techniques used. In general, there are three types of lithography, namely, optical lithography, x-ray lithography and electron beam lithography, which used different light sources. Photolithography involves multiple steps in which

the pattern on the mask is transferred onto a layer of photoresist [74,75]. Exposure of the photoresist causes chemical changes in which the resist either becomes insoluble (negative resist) or more soluble (positive resist). After the pattern transfer, chemical etching techniques are used to remove the exposed portion of the substrate which corresponds to the open hole (for negative resist) or a resist pedestal (for positive resist). With the current limits for photolithography, submicron level features can be realized easily. Although high resolutions of 90 nm can be achieved, the multistep process is time consuming and not suitable for efficient prototyping purposes. Nevertheless, there are many examples of glass microchips for electrophoresis separation [3–5] and microanalytical applications [6] which were fabricated using standard photolithography techniques.

Other combinations of novel materials and microfabrication techniques have also been developed. Networks of microfluidic channels of micrometer size can be fabricated by the micromolding in capillary (MIMIC) technique which employs an elastomeric (e.g. polydimethylsiloxane (PDMS)) master mold placed in contact with the prepolymer to be cured [76]. This simple technique is efficient and the mold can be reused many times. However, it can only be applied to low viscosity polymers which limits the selection of materials. An imprinting technique is able to fabricate complex micro-channel arrays by imprinting the plastic substrates (e.g. polymethyl methacrylate (PMMA)) using an inverse 3-dimensional image of the device micromachined on a silicon wafer [77]. Although this method is cost effective, the multiple steps process is not feasible for rapid prototyping.

More recent developments in the microfabrication methods are dominated by using polymers as the substrate material. Rapid prototyping has become a major challenge. Grzybowski et al. applied a low-power laser (10 mW) operating at 532 nm to ablate the desired pattern on PMMA, which was then transferred onto a PDMS master stamp for microcontact printing (μCP) or controlled sagging microcontact printing (CSμCP) [78]. This method defines a more rapid prototyping technique. However, it still involves a

multistep process and requires first creating the master stamp. A 3-dimensional PDMS microfluidic structure was developed by stacking several patterned PDMS layers [79]. Each patterned layer was fabricated by micromolding with a patterned silicon master. Oxygen plasma can be used to irreversibly seal PDMS with PDMS, glass, silicon or silicon oxide. Oxidation of the surface also supports electro-osmotic flow (EOF) and renders the surface hydrophilic (water liking) [80].

Beebe et al. used the technique of photopolymerization to construct microfluidic structures [81]. A reservoir with various depth was filled with a prepolymer mixture of momomers and a photoinitiator which was exposed to UV light through a photomask to define the micro-channel structures. This method is efficient with the drawback of numerous chemical processes involved. Microstereolithography also employs the technique of photopolymerization with the exception of using a focused laser beam to polymerize the 3-dimensional structure desired [82].

Laser photoablation is a technique which uses high energy photons to dissociate materials from the substrate. It provides a direct and rapid prototyping method for defining desired patterns and microfluidic structures. The high energy photon (7.9 eV) from the F_2 laser drives strong interactions in glasses for smooth and crack-free shaping of microchannels, microvias and arrays [83]. ArF excimer laser with a wavelength of 193 nm has also been employed to ablate micro-channels in PET (polyethylene therephthalate) [84].

2.3.2 Designs and Applications

There is a vast range of applications for such mini, lab-on-a-chip devices. Most applications are directed toward the field of biology and biomedical devices. Significant effort is focussed on DNA separation and sequencing, polymerase chain reactions (PCR), and cell handling. A few examples of the published work on lab-on-a-chip devices are presented here.

DNA separation and sequencing are two of the most popular biochip applications.

These capabilities are significant tools in the advancing fields of genomics and bioinformatics, which are the forefront of modern biology and life sciences research. Shi et al. demonstrated a radial capillary array electrophoresis microplate with a 10 cm diameter for high throughput DNA analysis which contained 96 microfabricated channels to separate 96 alleles in parallel [85]. Ueda et al. demonstrated a microfabricated separation chip with a 6 mm long channel and a laser-induced fluorescence detection system that was able to separate triplet repeat DNA fragment and DNA molecular marker within 12 s. This capillary electrophoresis device was at least 18 times faster than conventional capillary electrophoresis [86].

Rapid DNA sequencing is yet another important application for biochips. With the Human Genome Project being the catalyst, rapid DNA sequencing with high throughput was made possible by microfabricated electrophoretic devices. Liu et al. performed an optimization investigation of DNA sequencing separations in microfabricated electrphoresis channels. A complete run of sequencing separation of 500 bp with an accuracy of 99.4% was obtained in 20 min [87]. High throughput and rapid DNA sequencing was performed by Paegel et al. by developing a microfabricated 96-lane radial capillary array electrophoresis (μCAE) micro-channel plate. The device was able to sequence at a rate of 1.7 kbp/min which was a 5-fold increase over commercial technology [88].

PCR is a popular technique for amplification of DNA from as little as several strands to create thousands of replica copies. A demonstration of a compact real-time PCR instrument with two reaction modules allowing different temperature profiles and detection schemes for four-color fluorescence detection was developed by Belgrader et al. [89]. Waters et al. demonstrated a thermally cycled microchip which integrated thermal cell lysis, multiplex PCR amplification and electrophoretic analysis for sizing with intercalating dye for fluorescence detection [90]. Khandurina et al. [91], which was basically the same research group, demonstrated a PCR-based analysis on a microchip which employed a compact thermal cycling assembly with a microchip gel electrophoresis

platform. Each DNA amplification cycle required only ~1 min and as few as 10 thermal cycles were needed for detection, yielding a total analysis time of less than 20 min [91]. These devices, which incorporate sample preparation (cell lysis), reaction (DNA amplification), diagnostic (fluorescence detection) and analysis (electrophoretic sizing), are a good example of biochip applications.

Cell handling is a major part of the lab-on-a-chip development effort since an effective way of cell sorting and separation could potentially speed up the analysis process. Fu et al. demonstrated a disposable microfabricated fluorescence-activated cell sorter (mFACS) which was able to separate E. coli cells expressing green fluorescent protein from nonfluorescent E. coli cells. The cells were manipulate with electro-osmotic flow controlled by electrodes. The electro-osmotic potentials were computer controlled by the feedback received from the fluorescent emission collected by a microscope [92]. Arai et al. developed a system for cell isolation and separation of a single living cell in a microfluidic device under the microscope by integrating the laser-trapping and dielectrophoretic forces in 20 s [93]. With this system, only the desired cells are selected for culture or other diagnostic purposes.

Although these biochips operate efficiently with high performance, most still require external diagnostic tools which are large and bulky. More effort is required to miniaturize all diagnostic equipments for a true biochip that puts the whole laboratory onto a single chip.

2.4 Biophotonics – A Marriage of Photonic Technology and Biological Analysis

Biophotonics represents the extension of photonics technology to serve applications in biology. Biophotonics is a fusion of photonics and biology harnessing light for optical diagnostics, analysis, and light-activated and light-guided therapy. Biophotonics has

been at work since the beginning of time. Our lives depend on the energy of sun which has an abundant amount of light energy. Biophotonics is the basic building block of life and includes photosynthesis and vision, which convert photons into compounds for survival of plants and images for living beings, respectively.

This exciting field is truely a multi-discipline field which combines biotechnology, photonics, lasers and nanotechnology. Although the main thrust in each of these four fields are developing independently, their fusion truely offers great opportunities for engineers, biologists, chemist, physicist, medical personnel and researchers to work in a multi-discipline area with expertise drawn from each field.

2.4.1 Biophotonic Lab-on-a-Chip

The lab-on-a-chip is a very powerful tool that offers enhanced diagnostic sensitivity for small volume samples, miniaturization of large instrumentation, and high-speed and throughput for a vast number of applications. Integrating photonic functions into a lab-on-a-chip structure will improve its overall capability especially for detection, diagnostics and analysis of bio-samples. Biophotonic lab-on-a-chip will eventually be commercialized and widely used in laboratories and eventually in people's homes.

Many published papers have been focused on electrophoretic and electro-osmotic lab-on-a-chips combined with a separate optical system for detection and analysis [85–88, 92, 93]. Ocvirk et al. employed a confocal epifluorescence detection method to detect fluorescein within an electrophoretic micro-channel using a 488 nm argon ion laser excitation source [94]. Using a 635 nm laser diode, Jiang et al. demonstrated a highly sensitive laser induced fluorescence (LIF) detection on a planar microfluidic capillary electrophoretic chip with a confocal epiluminescent method and a photomultiplier tube [95].

Although this concept provides a practical detection and analytical method, there is a drawback in terms of packaging. The alignment and mechanical stability become

difficult and free space optics are not readily miniaturized.

Recent literature [7,8,96–101] has shown an increased research effort in microfabrication of biochips with photonic components. While such preliminary efforts are underway, the potential of biophotonic lab-on-a-chips remains untapped since biophotonics is still in an early stage of development. Biophotonic chips have the potential to revolutionize the way biology laboratories are designed, and less space and time are required to perform the same work.

Fabrication of integrated microanalytical devices with micro-channels and buried waveguides in flame hydrolysis deposited (FHD) glass was demonstrated by Ruano et al [7,8]. A simple fluorescence measurement was conducted to illustrate the sensitivity of this potential application with a minimum measurable concentration of 30 μM of Cy5 [7] and later a minimum concentration of 20 pM [8] can be measured. Mogensen et al. [96] demonstrated multimode buried-channel silicon oxynitride (SiO_xN_y) waveguides integrated with micro-channels for absorption measurement of a β-blocking agent, propranolol, at 212-215 nm. A detection limit at a concentration of 13 μM was reached which illustrated a sensitive integrated biochemical microsystem built as a lab-on-a-chip [96]. Furthermore, Hubner et al. obtained a minimum detected concentrations of 250 pM for fluorescein and 100nM for Bodipy (a special dye from Molecular Probes) using a transportable miniaturized fiber-pigtailed micro-system [97]. Polymer materials have become a material of choice for fabricating biophotonic lab-on-a-chip. Mogensen et al. [98] and Lin et al. [99] demonstrated SU-8 fabricated micro-device with integrated optical waveguides and micro-channels for fluorescence detection.

Another application for biophotonic lab-on-a-chip is flow cytometry. Friis et al. presented an unique layout for integrating waveguides and micro-channels which prevented leakage and hermetically seal the channels. Both absorption measurement and flow cytometry systems were demonstrated with fluorescent stained polymer beads [100]. A simpler design integrating pairs of optical fibers by fixing them in the grooves in the walls

of a micro-channel was able to detect single particles using light scattering or fluorescence emission [101].

The examples presented here are only a small portion of all the published work in the biophotonic lab-on-a-chip. However, they offer a glimpse of what is expected in the near future and as various potential applications emerge commercially. The future objective is to integrate optical functions and photonic capabilities together with microfluidic structures and analytical chambers to realize the full potential of biophotonics lab-on-a-chip technology.

2.4.2 Conclusion

The availability of various lasers has been the major contributing factor in the advancement of laser microfabrication. Direct laser processing provides a means for laser ablation and welding. It allows high precision, rapid throughput, and small heat affected zones to minimize distortion and change in material. These main advantages have led to the development and usage of a variety of laser systems for micromachining and processing. With the discovery of photosensitivity, direct laser writing of optical circuits and waveguides was made possible. With the direct laser writing technique, it does not only allow rapid prototyping of photonic components, it also provides a research tool for fabrication of complex micro-structures.

A biochip is a miniature laboratory with integrated capabilities from sample preparation to diagnotics and analysis. It offers enhanced measurement performances and has been applied in biology including DNA separation and sequencing, PCR, and cell separation and sorting. Integration of photonic components including waveguides and Bragg gratings greatly improves the diagnostic capability. Hence, the biophotonic lab-on-a-chip is the logical step forward. Its vast potential not only offers many biological applications, it will also revolutionize the design of laboratories.

Chapter 3

Biochip Design and Fabrication

This chapter presents the design of biochip components and the experimental arrangement. The fabrication and analysis of the lab-on-a-chip components and lab-on-a-chip devices are described and discussed. A F_2-laser system was used exclusively for micromachining and refractive index modification. Laser fabricated optical circuits were characterized by both free space optics and optical fiber probing.

3.1 F_2-Laser Microfabrication

3.1.1 F_2-Laser System Overview

A Lambda Physik LPF 220i F_2 laser and optical projection system shown in Figure 3.1 was the main instrument employed in fabrication of most biochip components. The laser generates radiation at 157 nm with single pulse energy of ~30 mJ. The pulse duration is ~15 ns and the repetition rate ranges from 1 Hz to 200 Hz. The non-uniform laser beam produced directly from the laser has a beam area of 5 mm x 22 mm. The beam has a divergence of 3 mrad and 1 mrad in the horizontal and vertical axes, respectively. The non-uniform beam passes through the MicroLas optical processing system.

The optical processing system rests on top of a floating optical table to damp external

vibrations and enable sub-micron alignment precision. A constant supply of high purity nitrogen gas was boiled off from liquid to purge the optical processing chamber and ensure efficient transmission of the 157nm light. An attenuator was used to vary the laser fluence from 10% to 70% by angle tuning two dielectric-coated CaF_2 mirrors. Following the attenuator, the non-uniform laser beam was vertically expanded 3-fold through a prism expander followed by a set of four sets of 9 x 9 lens arrays which homogenized the beam. The homogenized beam of 5 mm x 5 mm area provided uniform illumination of the mask with less than 5% variation. A Schwarzchild lens with 0.4 numerical aperture demagnified the mask image by 25 times at the target plane. The target sample was positioned by a computer controlled *xyz* precision stage (Newport TSPI100) with a resolution of <0.5 μm. A stream of nitrogen gas from the end nozzle (see Figure 3.1) provided a transparent optical beam path to the sample which was located in air for convenient mounting. A more detailed description of the system can be found in Herman et al. [102].

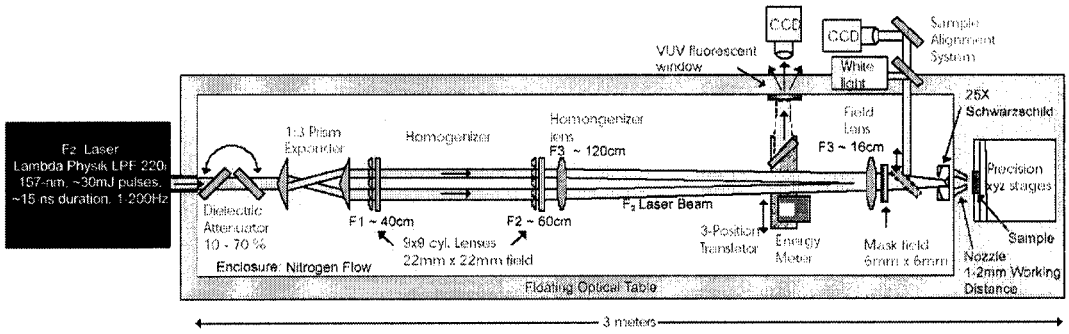

Figure 3.1: Lambda Physik LPF 220i F_2 laser (left) followed by the MicroLas optical processing system (right) and a computer controlled *xyz* target motion stage.

3.1.2 F_2-Laser Sample Holder

One important component in the F_2-laser microprocessing system is the sample holder. For the present project, a custom made sample holder (Figure 3.2) was designed and fab-

ricated for precise alignment registration for machining microfluidic channels and writing waveguides while a back pressure plate (Figure 3.3) was used for laser welding of glass samples. The main mount provided a vertical slot (10 mm x 3 mm) against which the glass was mounted to enable precise registration to the best-focus image plane of the laser beam. The back plate could be tightly mounted with three screws placed in a triangular arrangement to sandwich one or more glass samples. The surfaces of the holder were polished for flatness and orthogonality such that glass surfaces were reproducibly aligned to the laser image plane. The holder was made of magnetized stainless steel so that glass samples could also be mounted simply with a magnet.

Figure 3.2: Design details of the main sample holder which contains various holes through which the laser beam enters. Three threaded holes are used for screwing in the back pressure plate. All measurements are in mm.

The vertical slot (10 mm x 3 mm) at the bottom of the sample holder was designed specially for waveguide writing. The glass sample was placed on the polished bottom against the slot face to ensure that the motion stage formed waveguides parallel to the glass sample surfaces. This is necessary for waveguide characterization in which a perpen-

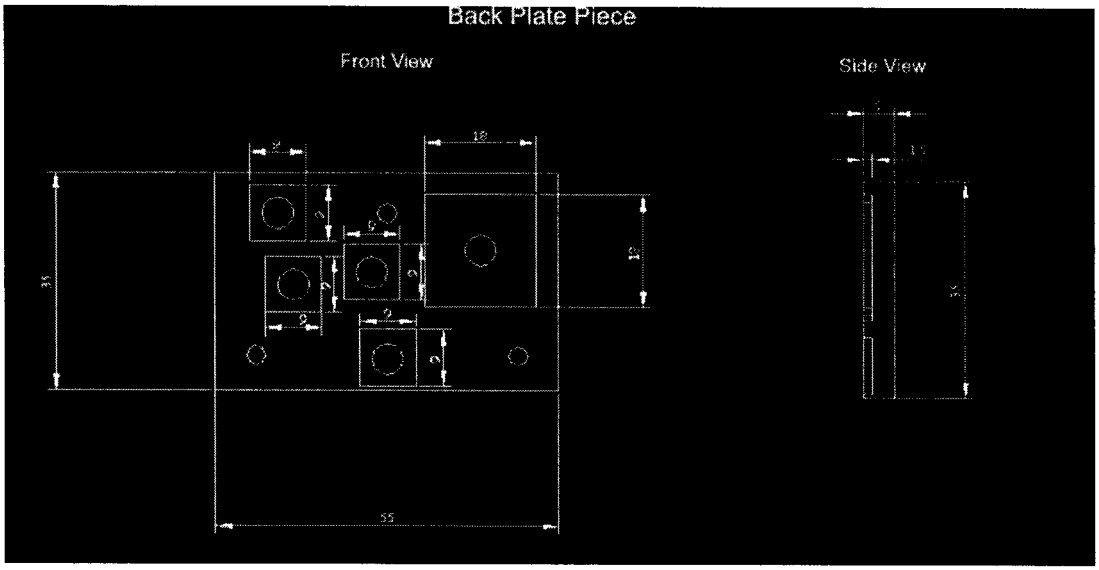

Figure 3.3: Back pressure plate for mounting to the sample holder (Figure 3.2). Depressions align with the laser port holes in the sample holder piece to prevent damage to the glass sample from laser-plasma generation on the back plate. Each depression also has a threaded hole to apply pressure to glass samples to be laser welded. All measurements are in mm.

dicular waveguide minimizes coupling loss and simplifies the optical coupling alignment.

The sample holder and back pressure plate improved the precision for secure mounting of samples that was not possible with the previous use of a magnetic holder. Large mechanical pressure could also be applied between two glass samples to ensure the close contact necessary for bonding by laser welding. The back pressure plate had depressions aligned with the laser port holes in the sample holder piece to prevent damage to the glass sample from laser-plasma generation on the back plate. Further, each depression had a threaded hole to apply additional pressure to glass samples to be laser welded. These depressions are also intended for ablation debris to escape from back surface ablation and to prevent laser ablation at the pressure plate from damaging the backside of samples.

3.2 Microfabrication of Lab-on-a-Chip Components

3.2.1 Ge-doped FHD Silica-on-Silicon Surface Optical Circuits

Optical waveguides and Y branches were formed in Ge-doped planar silica by F_2 laser radiation. Ge-doped flame-hydrolysis deposited (FHD) silica was fabricated and patterned with a NiCr mask by Alison Cleary from the University of Glasgow. The exposure of the FHD sample under F_2 laser through the NiCr mask was done at University of Toronto.

3.2.1.1 Fabrication of Ge-doped FHD Silica-on-Silicon Sample

The fabrication of the Ge-doped FHD silica samples with a NiCr mask involved several processing steps including electron beam writing and wet etching. A 100 nm thick NiCr patterned mask was fabricated directly onto the FHD silica sample to serve as a contact mask for defining waveguide exposure areas for the F_2 laser. There are advantages to this contact mask and laser exposure method. The first is that separate mask plate is not required for defining the patterns since a direct electron beam writing technique is used. The second advantage is that a preproduction of a CaF_2 mask with desired patterns is not necessary for F_2-laser irradiation since the mask is attached directly to the sample. The third advantage is that the pattern position is aligned precisely during the e-beam writing and further alignment is unnecessary. Moreover, this method provides a rapid, efficient and cost effective mean of prototyping any optical circuit onto Ge-doped FHD silica for each design iteration.

The Ge-doped FHD silica-on-silicon were prepared with three different germanium germanium concentrations of 3, 7 and 10 wt% in the top guiding layer which was 2 μm thick. Boron co-doping was used in the FHD process. Previous work by Marques et al. has demonstrated refractive index modification and preparation details of FHD silica [103]. Prior to defining the waveguide and Y-branches in the NiCr mask, Optiwave BPM simulations were done to predict single mode guiding at 632.8 nm. Detailed descriptions

can be found in the PhD thesis of Cleary [104].

Waveguide and Y-branch patterns were defined on samples using electron beam lithography of PMMA. This allows precise transfer of the desired pattern onto the NiCr mask onto the FHD silica. The resolution of the electron beam writer was set at 0.3125 μm which is more than sufficient to define 4 μm wide waveguides and 2 μm wide asymmetric Y-branches. Figure 3.4 summarizes the mask fabrication steps which include the following:

1. Clean the Si/SiO_2/FHD substrate.
2. Spin a layer of PMMA 2010 follow by 1 hr baking @ 180°C.
3. Spin a layer of PMMA 2041 follow by 1.5 hr baking @ 180°C.
4. 30nm NiCr coating to prevent substrate charging.
5. Expose the reverse of the waveguide pattern using electron beam writer.
6. NiCr is removed prior to PMMA development.
7. 100nm NiCr coating on the sample.
8. Lift off the remaining PMMA in the patterned region and irradiate the NiCr patterned FHD with the 157nm laser.

Detailed procedures for contact mask fabrication are provided in reference [104].

All the FHD silica samples were 1 cm x 1.5 cm x 2 mm and fabricated with three sets of identical waveguides and Y-branches having lengths of 1 cm. Figure 3.5a shows a FHD silica sample with NiCr waveguide patterns. Figure 3.5b is an enlarged image of a Y-branch which shows an accurate reproduction of the apex of the Y-branch that was formed by e-beam:PMMA technique. Photolithography often does not give such accurate reproduction.

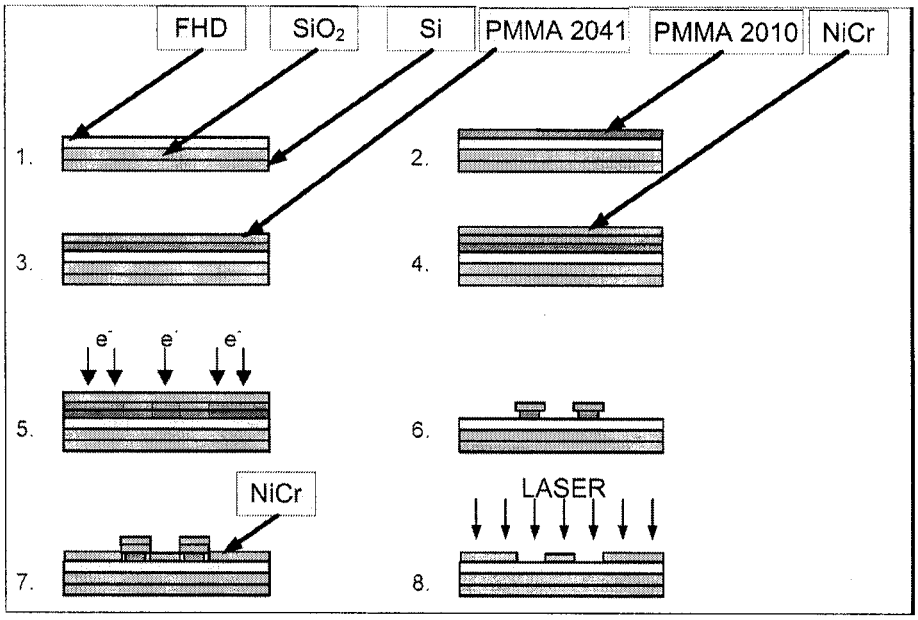

Figure 3.4: Contact masks were defined on the FHD silica surface using electron beam lithography of PMMA followed by deposition of 100nm thick NiCr. A lift-off process was employed to remove the composite PMMA-NiCr over-coating, thereby defining patterns to receive laser exposure [104].

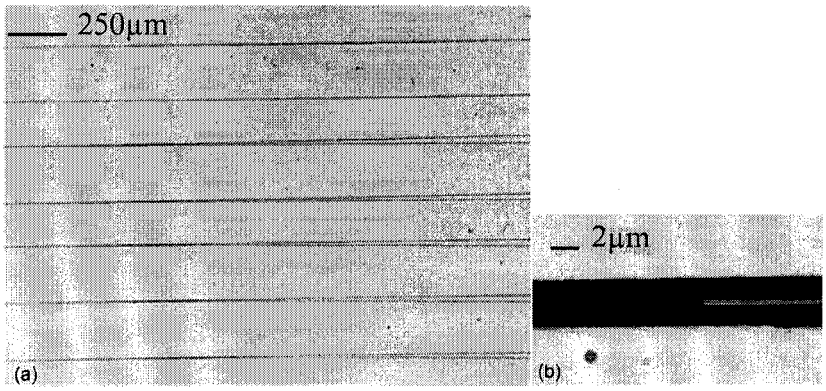

Figure 3.5: Microscope image of the NiCr mask prior to F_2 laser irradiation: (a) Straight waveguides followed by Y-branches and (b) showing the apex of a Y-branch [104].

3.2.1.2 Refractive Index Modification by F_2-Laser exposure

Various straight waveguides and Y-branches were directly irradiated through the NiCr patterned Ge-doped FHD silica by the F_2 laser light. The configuration of the experimental setup for mounting and exposing FHD samples is shown in Figures 3.6 and 3.7.

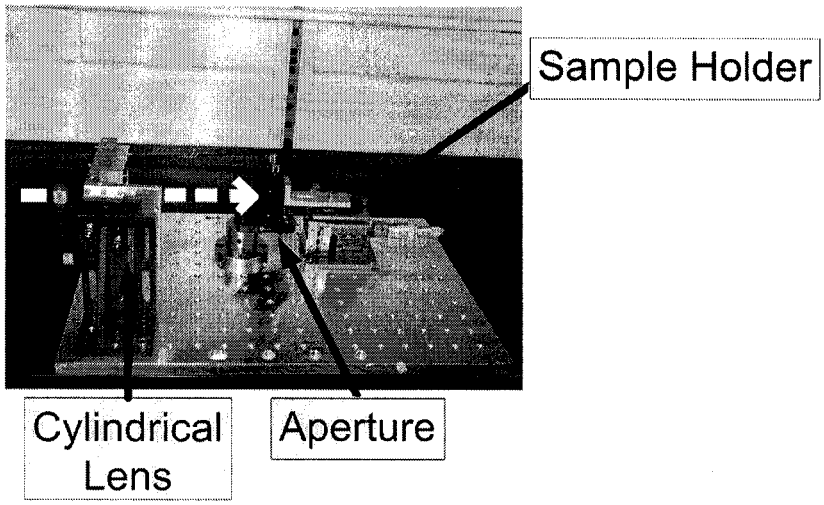

Figure 3.6: A photograph of the experimental setup for laser exposure of waveguides and Y-branches in a FHD Ge-doped silica planar substrate. The dashed line shows the laser beam path through a cylindrical lens, and an aperture, before exposing the sample.

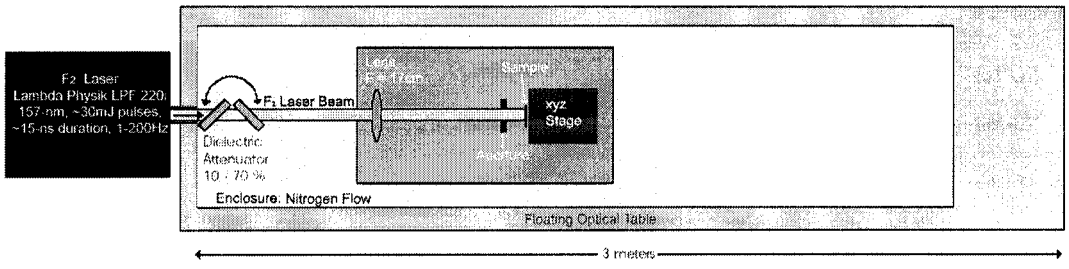

Figure 3.7: Schematic of the experimental arrangement for writing waveguides and Y-branches. The optical breadboard, which consists of a cylindrical lens, an aperture and xyz precision stage, was placed inside the nitrogen purged processing chamber.

An optical breadboard (Figure 3.6) assembled with a cylindrical lens (focal length = 17 cm), an aperture and a *xyz* stage for sample alignment was placed in the nitrogen purged laser processing chamber as shown in Figure 3.7. The cylindrical lens concentrated the laser beam onto the open mask areas of the sample which was aligned by the *xyz* stage. The aperture further restricted the exposed area on the patterned NiCr mask FHD sample to one set of waveguides/Y-branches. The sample was aligned prior to gas flushing and further alignment was also possible by using the gloves to access the inside of the chamber.

Several waveguide samples were exposed by the F_2 laser. Three FHD samples with Ge-doped concentrations of 3%, 7% and 10% (wt%) were tested. After the irradiation, the NiCr was etched with a standard Cr etch solution.

3.2.2 F_2-Laser Welding

Laser welding of optical glasses remains a challenging area today because of the weak optical absorption available with most commercial lasers and the brittle nature of glass. The 157 nm F_2 laser was selected for the wide processing window that drives strong absorption at high fluence exposure larger than 1 J/cm^2 without inducing microcrack formation. The method of second surface ablation was applied to the contact point between the glass plate and glass fiber to locally heat, melt, and reflow the glass and thereby weld together the two similar glasses as shown in Figure 3.8.

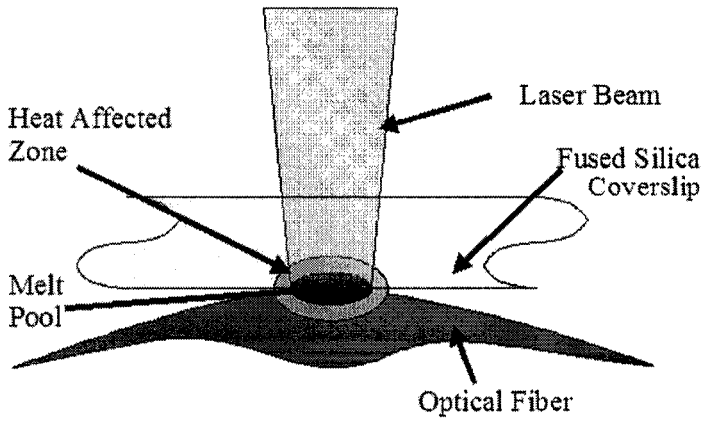

Figure 3.8: Arrangement for laser welding. Laser beam induces strong absorption of second surface of substrate at contact point with curved weld sample (optical fiber). The melt pool fuses the front and back material together.

Figure 3.9 shows the schematic of the laser welding setup. The laser beam was scanned along the fiber to the substrate contact surface to produce a line of overlapping welds of 25 μm. Fused silica samples of up to several hundred microns thick could be welded owing to a ~100 nm thermal diffusion scale length [105]. Mechanical pressure was applied to the samples to ensure contact of the laser formed melt necessary for welding.

A fused silica coverslip (160 μm thick) was placed vertically in the sample holder as shown in Figure 3.9 with two identical SMF-28 fibers placed parallel to provide two high pressure contact points.

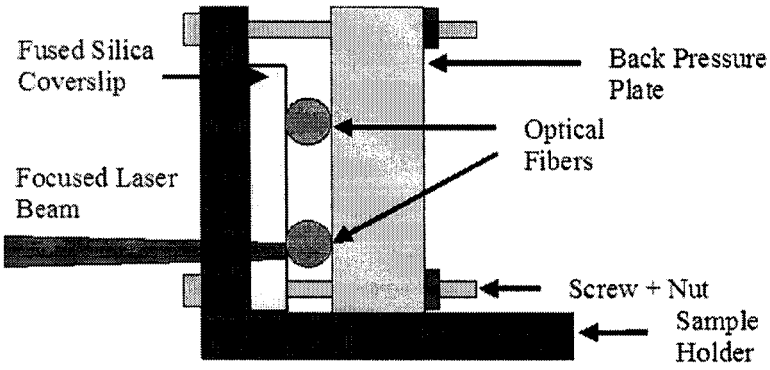

Figure 3.9: Laser welding arrangement showing a fused silica coverslip and two optical fibers pressed in contact by the sample holder and back pressure plate.

3.2.3 Waveguide Intersecting Microfluidic Channels

F_2-laser micromachining and refractive index profiling were combined to enable single-step integration of photonic devices with microfluidic functions on a single chip. Optical waveguides were written to intercept microfluidic channels for optical sensing of cells. An integrated biosensor was fabricated and optically characterized for insertion loss and sensitivity to detecting polystyrene microspheres.

3.2.3.1 Buried Waveguide Writing

When the laser fluence is below the ablation threshold, refractive index modification can be induced near the surface of glasses. Above the ablation threshold, material dissociation and surface micromachining result. However, efficient refractive index modification can also result at such high fluence when the laser focus is sufficiently deep inside the substrate

material [49].

F_2 laser exposure of fused silica can yield buried refractive index modification of up to $5x10^{-3}$. A hole-arrayed aluminum mask was placed at the mask field to project a linear line of focal spots inside the fused silica sample by the Schwarzchild lens (25x demagnification). The mask had an array of squares of 0.15 mm x 0.15 mm (Figure 3.10) that was demagnified to 6 μm x 6 μm.

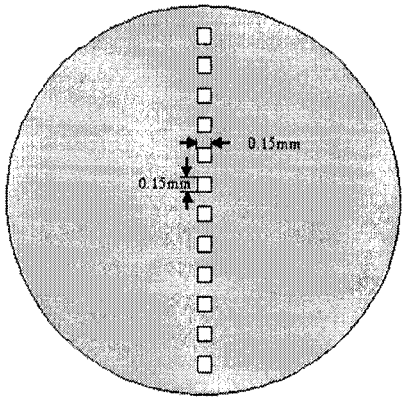

Figure 3.10: Aluminum mask with array of 0.15 mm x 0.15 mm squares used for F_2-laser waveguide writing.

There are three reasons for using an array of square apertures. First, each square independently focus with 2-dimensional scaling to provide a small depth of focus. Second, an array of these squares better uses the available laser energy for a faster writing speed comparing to single square mask. Thirdly, the array of squares, positioned vertically as shown in Figure 3.10, could be scanned at an offset angle controlled by the *xyz* stage such that symmetric waveguides (width equals depth of focus) were formed. A 6 μm wide line of refractive index modification was formed. Several important factors controlling the waveguide properties are the laser energy and fluence, the waveguide depth, the mask geometry and the sample translation speed.

3.2.3.1.1 Laser Fluence Laser energy was carefully measured as one part of determining the on-target laser fluence. An energy detector (Molectron J25LP-MB-1187) was placed at the output nozzle of the processing chamber and in the nitrogen gas stream to create an optically transparent path for the focusing 157 nm laser beam. The on-target beam area was confined by the aperture(s) on the aluminum amplitude mask. An on-target fluence range of 1 to 5 J/cm^2 (energy over area) was available for writing waveguides and micro-channels. A three hour nitrogen gas purge was required to displace the air and moisture from the processing chamber, which together with one hour of laser warmup would provide steady energy throughout long 12-hour experiments. Another power detector (Molectron J50LP-4-OAO) positioned before the mask field was used to measure the energy inside the chamber to crosscheck the energy measured at the nozzle.

When a gas mixture of F_2 and He was used, a secondary red line would contribute 10-20% of the total measured energy. A gas mixture of F_2 and Ne did not produce red emission and required no correction of measured energy. F_2 and Ne gas mixture were used for the majority of the experiments.

For waveguide writing, the laser beam was focused inside the fused silica block with fluence values above the ablation threshold of 1 J/cm^2. In order to estimate the internal fluence, Fresnel reflection and sample absorption was taken into account in the energy determination according to:

$$E_{target} = (1 - P_{red}) * (1 - (\frac{n_{SiO_2} - n_{air}}{n_{SiO_2} + n_{air}})^2) * e^{-\alpha d} * E_{measured} \tag{3.1}$$

where E_{target} is the laser energy appearing at the focal spot, P_{red} is the percentage of red energy in the laser beam (15% or 0% for He or Ne buffer gas, respectively), n_{SiO_2} (= 1.69 at 157 nm wavelength) is the refractive index of fused silica, n_{air} (= 1) is the refractive index of air, α = 10cm^{-1} is the absorption coefficient, d is the depth of the focused beam and $E_{measured}$ is the energy measured at the nozzle.

3.2.3.1.2 Waveguide Depth Determination of the waveguide depth required a correction for refraction due to the air to fused silica interface according to:

$$d = \frac{ztan(sin^{-1}(\frac{N.A}{n^2_{SiO_2}}))}{tan(sin^{-1}(\frac{N.A}{n_{SiO_2}}))} \tag{3.2}$$

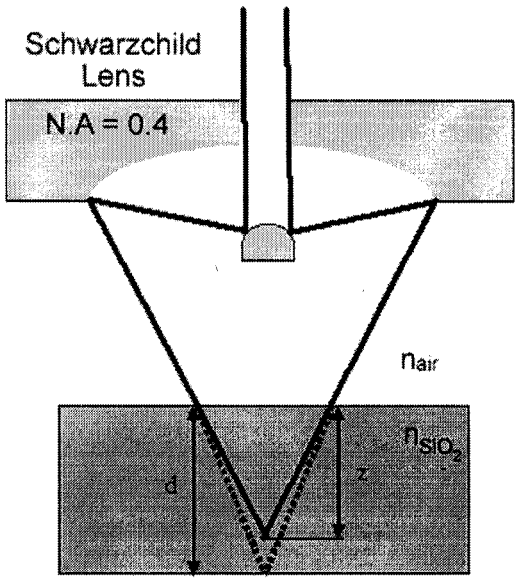

Figure 3.11: Illustration of ray trajectories for determination of waveguide depth. The solid and dotted lines represent the ray trajectories without and with refraction correction, respectively.

where d is the physical depth of the laser spot from the surface, z is the depth without surface refraction and N.A is the numerical aperture of the Schwarzchild lens. Figure 3.11 shows the ray trajectories of the focus depth with (dotted line) and without (solid line) correction for refraction due to the air to fused silica interface. For a N.A of 0.4, Equation 3.2 yields:

$$d \cong z(0.558) \tag{3.3}$$

Waveguides were written in a range of 10 to 25 μm depth from the surface. It was necessary to keep the fluence at the surface below the ablation threshold. However, the focussing beam created a fluence above the ablation threshold inside the sample to efficiently create the refractive index modification.

For ' z' equal to sample thickness, equation 3.3 provides the sample displacement necessary to move the laser beam focus from the front to the back surface of the fused silica substrate. A micrometer was used to measure the thickness of fused silica slips to define ' z', and the calculation of ' d' provided the appropriate axial shift of the fused silica to induce backside ablation for welding to a second glass sample.

3.2.3.1.3 The Translation Speed The sample translation speed depended on the required fluence per pulse, mask open area and the net fluence required. The computer controlled xyz stage translated the sample vertically, orthogonally to the laser beam direction, with the scanning speed defined by:

$$v_s = \frac{L * F_{target} * f_{rep}}{F_{net}} \tag{3.4}$$

where L is the integrated illumination length of the focused array of squares on target, F_{target} is the fluence per pulse on target, f_{rep} is the repetition rate of the laser, and F_{net} is the net fluence desired.

A constant scanning speed was used to generate an uniform line of refractive index modification. Microcracks were not observed within, or near, the written waveguides which is necessary to avoid high scattering losses by the guided light.

3.2.3.2 Microfluidic Channel Ablation

Micro-channels were ablated by focusing a square 30 μm x 30 μm beam onto the fused silica sample. This beam was created with a 0.75 mm x 0.75 mm amplitude mask as show in Figure 3.12. The glass sample was translated at a constant speed along a direction

parallel to one of the straight beam edges to ablate a rectangular shaped micro-channel.

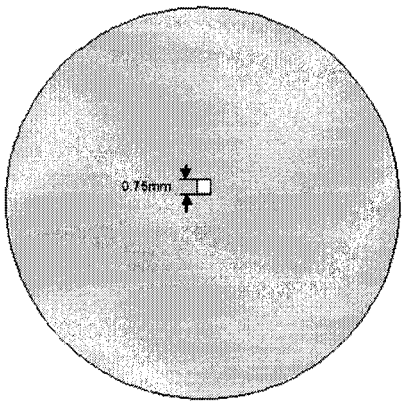

Figure 3.12: Aluminum amplitude mask with a 0.75 mm x 0.75 mm square aperture used for micro-channel writing.

The resulting channels yield high steepness with a width of 30 μm in various depths of 1 to 40 μm. The depth, D, was controllable and defined by the following equation:

$$D = \frac{B_{etch} * f_{rep} * L_{feature}}{v_{etch}} \tag{3.5}$$

where v_{etch} is the scanning speed for etching, B_{etch} is the single-pulse etch rate for a given laser fluence, f_{rep} is the repetition rate of the laser, and $L_{feature}$ is the size of the laser beam projected along the channel direction. A range of experimental exposure conditions of B_{etch} = 0.080 to 0.130 μm/pulse, f_{rep} = 10 Hz, $L_{feature}$ = 25 to 30 μm and v_{etch} = 0.001 to 0.020 mm/s were investigated to optimize micro-channels for steep smooth walls without generating microcracks.

3.2.3.2.1 Fused Silica Ablation Fused silica ablation rates, B_{etch}, were determined for calibrating exposures to produce a desired micro-channel etch depth. Four fused silica samples were exposed to 2.42 J/cm^2, 2.89 J/cm^2, 3.39 J/cm^2, and 3.94 J/cm^2 fluence per pulse with scanning speeds in the range of 0.001 mm/s to 0.020 mm/s. The etch rates,

B_{etch}, were obtained from Equation 3.5 and the results are plotted in Figure 3.13. The etch rate follows an expected logarithmic dependence on the single-pulse fluence.

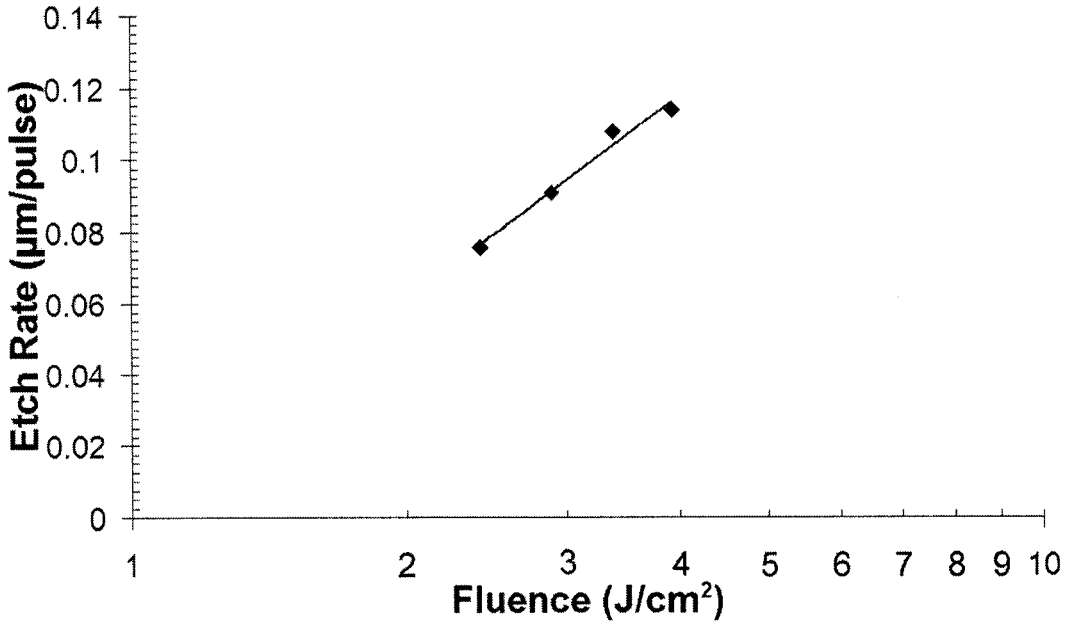

Figure 3.13: F_2 laser etch rate versus single-pulse fluence for fused silica.

The new rates are ~25-30% higher than previously published data on fused silica which are reproduced in Figure 3.14 [16]. Figure 3.14 also shows the single-pulse etch rates in UV grade fused silica by 193 nm radiation, and Ge-doped silica by 157 nm radiation.

Several factors may contribute to the higher etch rates observed in Figure 3.13. In the previous work, a laser gas mixture of F_2 and He [106] yields a secondary red line contributing 10-20% of the total measured energy that adds uncertainty to the energy measurement. The present laser exposures were based on F_2 and Ne mixtures which do not generate the red line. Energy detectors for 157 nm were not calibrated, and differ-

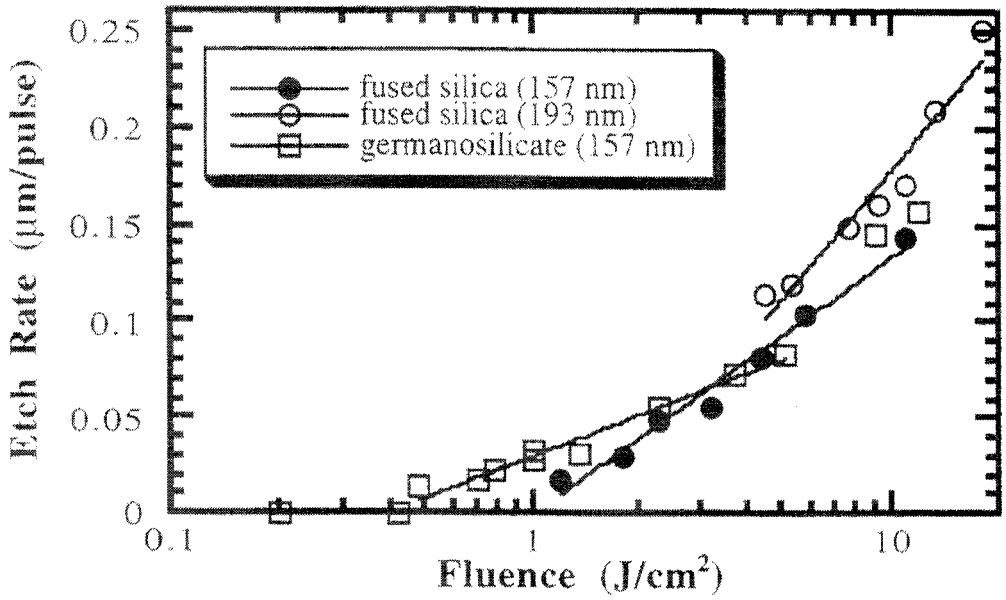

Figure 3.14: Single-pulsed etch rates of UV grade fused silica using 157 nm and 193 nm lasers. Ge-doped silica results are shown for 157 nm radiation. The figure is reproduced from Herman et al. [16]

ent model in past, Molectron JD500, versus Molectron J25LP-MB-1187 and Molectron J50LP-4-OAO currently, added further uncertainty to the energy calibration. Other factors affecting the etch rates and energy measurements include temperature, humidity, and ambient gas (i.e vacuum increases etch rates).

The fluence per pulse and ablation depth were two fundamental parameters which governed the smoothness and steepness of the micro-channel wall and the formation of cracks. Higher single-pulse fluence creates micro-channels with steeper and smoother walls as shown in the cross-section microscope images in Figure 3.15a and Figure 3.15b of 3.39 J/cm^2 and 2.89 J/cm^2, respectively. From Figure 3.15a, a higher fluence of 3.39 J/cm^2 yields a steeper wall slope of 11.7^o compared with 18.4^o from a fluence of 2.89 J/cm^2. The scan rates were 2 μm/s and 5 μm/s for the deeper and shallower micro-

channels, respectively.

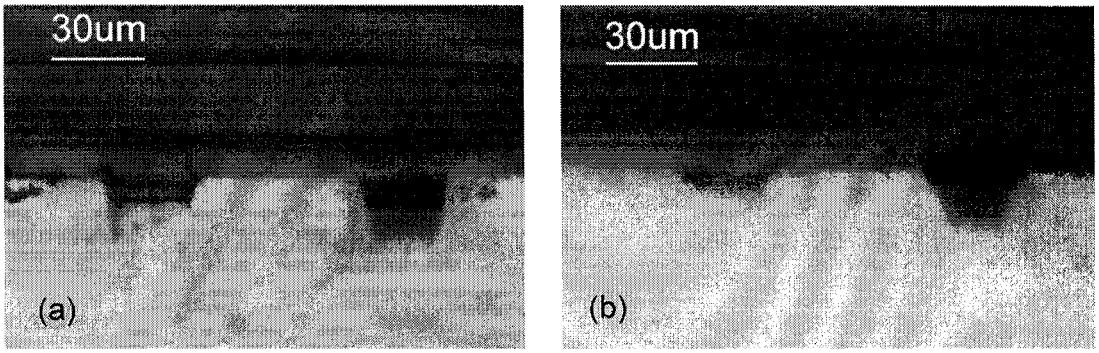

Figure 3.15: Cross-section optical microscope images of the micro-channels ablated with single-pulse fluence of: (a)3.39 J/cm^2 and (b)2.89 J/cm^2.

Vertical walled micro-channels are most desirable for waveguide coupling. Therefore, the highest available fluence of ~4 J/cm^2 was employed for all channel fabrication. Another factor was to avoid microcracks that can appear when etch depths exceeded the ~30 μm channel depth. As shown in Figure 3.16, the depths of the micro-channels were as follows:

All the micro-channels had sharp wall edges except the deepest one in Figure 3.16a which had a ~1:1 ratio for the depth to width. Further, optimization of the laser exposure conditions are necessary to produce higher aspect ratio channels without microcracks. For the present project, micro-channels were fabricated with high fluence of ~4 J/cm^2 and the channel depth was approximately the same as the width.

3.2.3.3 Integrated Waveguide and Micro-channel

The interception of a F_2 laser written waveguide with micro-channel was relatively straightforward since the processing window was known. Both components could be fabricated in a single step F_2-laser process by varying the image focal point between the surface of the fused silica glass for micro-channel writing and in the bulk fused silica for waveguide writing. However, waveguides were fabricated prior to cross ablation of

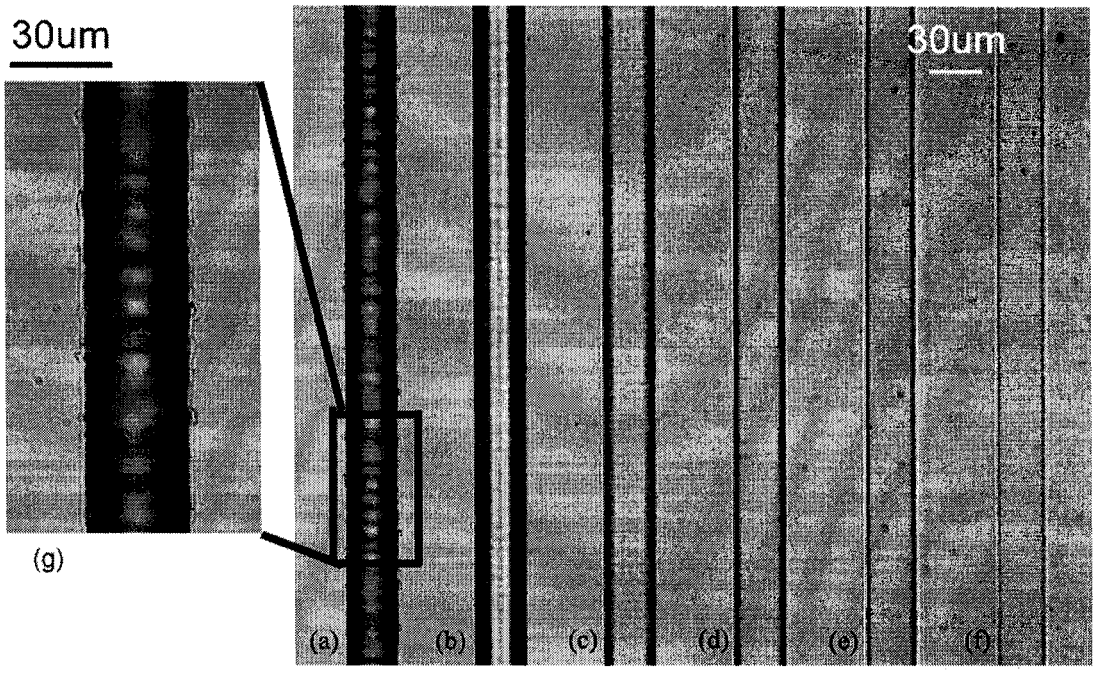

Figure 3.16: Top view images of the 30 μm wide micro-channels with various depths: (a) 30.75 μm (b) 16.07 μm (c) 4.35 μm (d) 2.33 μm (e) 1.51 μm (f) 1.16 μm. (g) is an enlarged image of micro-channel (a) in which microcracks are observed on the channel edges.

micro-channels in order that the waveguides could be optically characterized with and without an intercepting micro-channel.

Near surface buried waveguides were fabricated 10 to 25 μm deep to intercept micro-channels which could only be ablated to a depth of 30 to 40 μm for optimal particle detection results. Steep walled channels were necessary to reduce light loss from surface reflection. Smooth walls reduced scattering loss and fewer micro-cracks on the channel edges could provide better sealing of micro-channels. The designed channel depth of 30 to 40 μm ensured the waveguides intersect the micro-channels for the interrogation of particles and optimal signal detection through the waveguides.

3.3 Diagnostics of Integrated Optical Circuits

3.3.1 Near-Field Modal Profiling

The near-field modal profile of a buried waveguide can be used to obtain information about the refractive index modification. Hence, a diagnostic station was constructed specifically for waveguide characterization. The station was placed on top of a floating optical bench for vibration control.

A SMF-28 fiber was mounted onto a xyz stage (Melles-Griot Nanomax) and used to couple either red, or infrared, light into the laser-formed waveguides. The red and infrared laser sources were fiber coupled and provided 635 nm (Thorlabs Inc., S1FC635) and 1550 nm (Thorlabs Inc., S1FC1550) wavelengths. The waveguide sample was placed on stage with yz translation and vertical and horizontal tilting angle adjustments. With these degrees of freedom, both stages enabled effective alignment of the fiber sources into each waveguide of the sample. A CCD camera (Panasonic GP-KR222) was positioned on top of the diagnostic setup to aid in alignment. The image from the CCD was observed through a monitor and computer and could be used to capture images or videos. A zoom lens (2.5x to 10x) was attached to the CCD for controlling the image magnification.

Refractive index matching fluid (Cargille n = 1.46 at 589.3 nm) was applied on all the fused silica waveguide samples to compensate for the bevels on both the input and output surfaces. From the input side, the index matching fluid filled the air gap between coupling fiber with the waveguide input surface. On the output side, a microscope slip (sodalime, 160 μm thick) was held against the output surface by the viscous index matching fluid. The fluid filled the gap between the bevel on the sample edge and the glass slip to provide distortion-free modal profiling. Figure 3.17 illustrates the coupling arrangement.

The near field modal profile were captured through a 100x microscope objective lens (N.A = 0.95) which focused the image onto a Spiricon CCD (SP-1550M). A schematic of the diagnostic setup is shown in Figure 3.18. The Spiricon CCD was used to capture

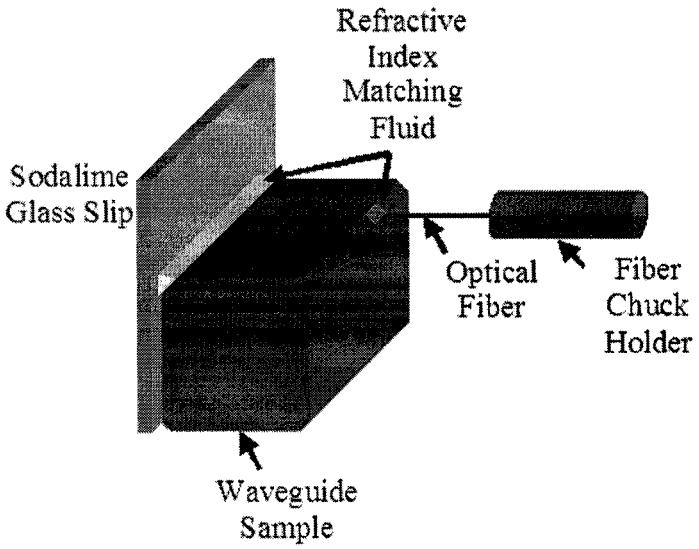

Figure 3.17: An illustration showing the use of refractive index matching fluid to efficiently couple light from the input optical fiber to the sample waveguides, and then out through the bevels for distortion-free viewing of the modal profile.

images in the visible and infrared spectrum to provide near-field modal profiles. A calibration factor corrected the difference between the CCD pixel size and the actual image size. The calibration factor was determined by imaging a glass plate with known line spacings through the same optical arrangement onto the CCD.

3.3.2 Insertion Loss Measurement

Insertion loss comprises of coupling loss, propagation loss, mode mismatch, scattering loss, and reflection loss. The total insertion was obtained by subtraction of a fiber-to-fiber reference signal with the signal measured from fiber butt coupling to the waveguide sample. This measurement was conducted for all waveguides fabricated. Refractive index matching was used as mentioned in section 3.3.1 in Figure 3.17 for minimizing coupling loss due to the roughness on the bevels.

The setup for insertion loss and spectral measurements was similar to the setup

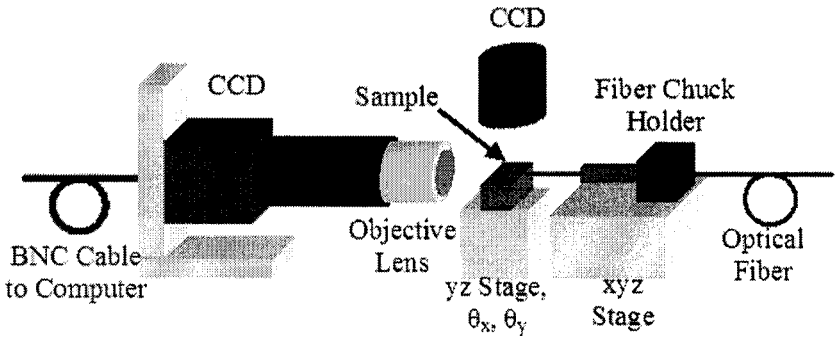

Figure 3.18: The diagnostic setup used to capture the near field modal profile.

in Figure 3.18 used for near-field modal profiling. The difference is that the CCD camera setup with the objective lens was replaced with a SMF-28 fiber butt coupled setup connected to either an OSA or optical power detector at the output facet of the waveguide sample. Three different input sources were employed: 635 nm (Thorlabs Inc., S1FC635), 1550 nm (Thorlabs Inc., S1FC1550), and ASE broadband light at 1.53 to 1.61 μm (Thorlabs Inc., ASE-FL7002). The spectrum of the ASE broadband source is shown in Figure 3.19.

When the output collection fiber positioned on a similar *xyz* stage (Melles-Griot Nanomax) as the input fiber, the insertion loss could be obtained in two ways. The first method used fiber coupled ASE source as the input light source and an optical spectrum analyzer (ANDO AQ6317B) at the output of the waveguide sample. The captured spectrum was compared to a reference spectrum acquired by coupling the input and output fibers closely together (less than 10 μm separation). It was done prior to every experiment to ensure accurateness. Spectral differences provided the total insertion loss. Moreover, all fiber ends were checked under a 10x magnification to observe damages including scratches and chipped ends. Fibers would be re-cleaved when damages were observed.

The second method used the red/IR light source as the input and power detectors

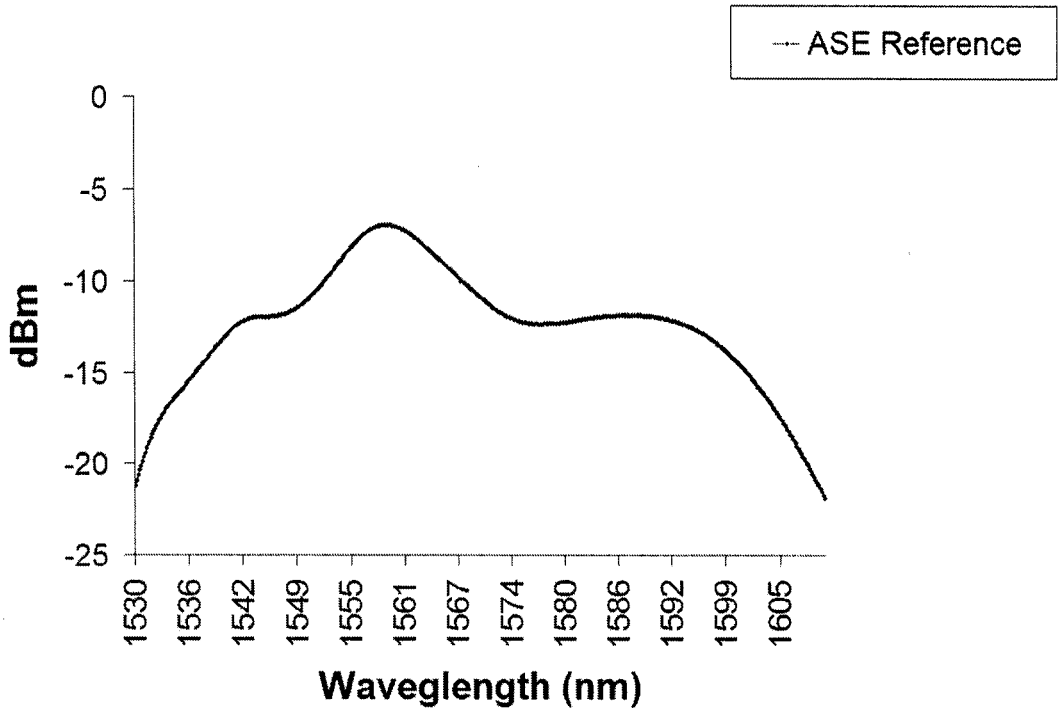

Figure 3.19: The power spectrum of the ASE (Thorlabs Inc., ASE-FL7002) broadband light source.

(Newport 818SL and 818IR) connected to a Newport multi-function optical meter (1835-C) at the output. A reference was obtained in a similar fashion as the previous method. Newport power detectors, 818SL and 818SL, were used to detect red and infrared light, respectively. Figure 3.20 illustrates the diagnostic setups for insertion loss measurement.

3.3.3 Propagation Loss Measurement

The insertion loss measurement of Section 3.3.2 consists of the following losses: coupling loss, propagation loss, mode mismatch, scattering loss, and reflection loss. A large loss component was due to the propagation loss.

As waveguide propagation loss can be measured in several ways. The method employed here used the diagnostic setup described in the Section 3.3.1 and shown in Figure

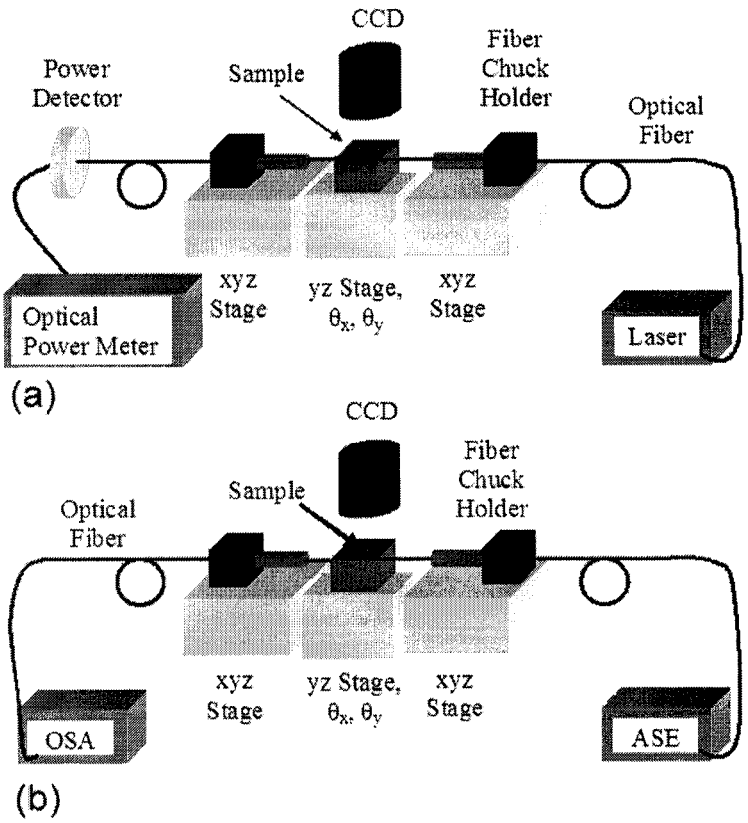

Figure 3.20: The diagnostics setup used for insertion loss and spectral measurements. (a) ASE input light source and an OSA at the output and (b) red or IR laser as the input light source and an optical detector connected to an optical power meter at the output.

3.18 to find the best input coupling by observing the near field modal profile at the output. A CCD camera (Panasonic GP-KR222) viewing the top of waveguide was used both for aiding the alignment process and for capturing the gray-scale images of scattered waveguide light. Waveguide losses were inferred from the exponential decrease in this scattered light with distance along the waveguide.

The captured images, with known scale and length measurements, were applied to calculate the propagation loss due to decrease of scattering light power which is proportional to the pixel value. The pixel values (black (0) to white (255)) along the optical propagation path were obtained to plot a scattering intensity as a function of distance.

The data obtained for the first and last 1 mm from the end facets of the waveguides were discarded due to the discrepancies caused by the reflection and scattered light. The best exponential fit curve was determined for each fabricated waveguide and this provided an estimate of the propagation loss.

For the present purpose of detecting polystyrene microspheres, propagation loss was only measured at the wavelength of 635 nm. The propagation loss at a wavelength of 1550 nm was not measured because the waveguides were designed for the use in detecting microspheres which are highly absorbing at visible and transparent in the infrared.

3.3.4 Refractive Index Characterization

Results of the near field modal profiling (Section 3.3.1) were used to calculate the laser induced refractive index modification that gives rise to the waveguides.

A method of mode profile simulation was applied by using a simulation package (RSoft Photonics CAD) to match the calculated refractive index profiles to observed profiles and provide an estimated refractive index modification in the red and infrared. Although the cross section of the waveguide observed under the microscope had an elliptical shape, a step-index profile at the focal point was used for simulation purpose to estimate the peak refractive index change. Since waveguides were written using a mask with an array of 6 μm x 6 μm squares, the simulated waveguide transverse width was set at 6 μm. Hence, an estimation of the peak refractive index modification could be obtained by varying the index contrast and fitting the observed mode profile.

3.3.5 Characterization of Integrated waveguides and Micro-channels

The near-field mode profile, the insertion loss with spectral measurements and the refractive index characterization of all F_2 laser formed waveguides were obtained prior to ablation of micro-channels across the waveguides. The insertion loss measurements were done before and after the micro-channels fabrication for the purpose of obtaining the loss

due exclusively to the micro-channel gap.

The integrated waveguide and micro-channel were next applied to sensing polystyrene microspheres with a $\sim$15 μm diameter. The spheres were moved through the micro-channels in distilled water by the capillary effect. Two methods were used to measure the detection of microspheres passing the intersecting buried waveguides. Both methods were similar as the insertion loss measurement described in Section 3.3.2. When the microspheres passed through the intersecting waveguides, a transmitted power drop expected due to scattering and occultation of transmitted light.

The method described in Section 3.3.2, which employed the laser sources, optical power detectors and meter, was more attractive because the power meter data could be collected on a computer through a GPIB connection at a frequency from 25 Hz to 200 Hz. For a fixed buffer size of 2500 data points, time events from 100 s to 12.5 s were determined.

Chapter 4

Results and Discussions – Laser Processes

In this chapter, F_2-laser micromachining results are presented. These results are for the basic components essential to microfabricate a biophotonics lab-on-a-chip. UV grade fused silica and Ge-doped FHD silica-on-silicon were used as substrate materials. Fused silica ablation data presented in Section 3.2.3.2.1 provides a controllable ablation depth of micro-channels. Survey experiment assesses the possibility on F_2-laser micro-welding of transparent glasses. Direct F_2-laser written buried waveguides in fused silica and Ge-doped FHD silica-on-silicon provide an optical platform for biophotonics lab-on-a-chip structures. These results define the fundamental laser processing windows for creating the building blocks of any biophotonics devices.

4.1 F_2-laser Welding of Glasses

4.1.1 Processing Window

Fused silica coverslips with thickness of ~160 μm were welded to SMF-28 optical fibers with a F_2 laser. A square aperture mask providing a spot size of 25 μm x 25 μm was

scanned along the back surface of the coverslips. The optical fibers contacting the back surface of the fused silica slip were fused at several contact points. If the fluence was greater than 3.8 J/cm^2, then the front surface would ablate prior to the onset of back surface ablation. If the fluence was under 2.1 J/cm^2, then the front and back surfaces were not ablated or melted. A narrow processing window was determined in which the back surface of the coverslip melted and flowed to fused with the optical fibers.

Ten melted lines, crossing two fibers perpendicularly on the back surface of the fused silica coverslip, were applied to weld the fibers at the contact points. Table 4.1 provides the fluence processing window showing successful fusing of coverslip to optical fiber. Distinct back surface melt lines were observed with a single-pulse fluence range of ~2.61 J/cm^2 to ~3.33 J/cm^2 which defined the narrow processing window of F_2-laser welding. Pronounced back surface ablation lines from ~3.66 J/cm^2 to 4.07 J/cm^2 generated back surface channels.

Table 4.1: Processing window of F_2-laser welding of fused silica coverslip with optical fiber.

Fluence per Pulse at nozzle (J/cm^2)	Welding Description	Weld (Successful/Unsuccessful)
2.08	faint back surface ablation/melt	Unsuccessful
2.61	faint back surface ablation/melt	Unsuccessful
3.31	distinct back surface ablation/melt	Successful
3.33	distinct back surface ablation/melt	Successful
3.66	pronounced back surface ablation	Unsuccessful
3.81	pronounced back surface ablation	Unsuccessful
4.07	front surface ablation	Unsuccessful

At the welded contact points, the melted glass flowed to fuse together the coverslip and the optical fiber. The criteria for successful welding was determined by a simple test. After laser welding, the fused silica coverslip was flipped with the fiber side down

and the optical fibers that remained stuck on the fused silica slip until a gentle pull were deemed successful welds. The optical microscope (Figure 4.1) and atomic-force microscope (AFM) images (Figure 4.2) show the welded contact points. Figure 4.1a and b show the fused coverslip and optical fibers with laser tracks. Figure 4.1c and d show magnified images of the fused silica coverslip surface and optical fiber surfaces after the optical fiber was pulled off which discloses the contact weld point, respectively. Figure 4.2 shows the AFM images of the weld point shown in Figure 4.1c.

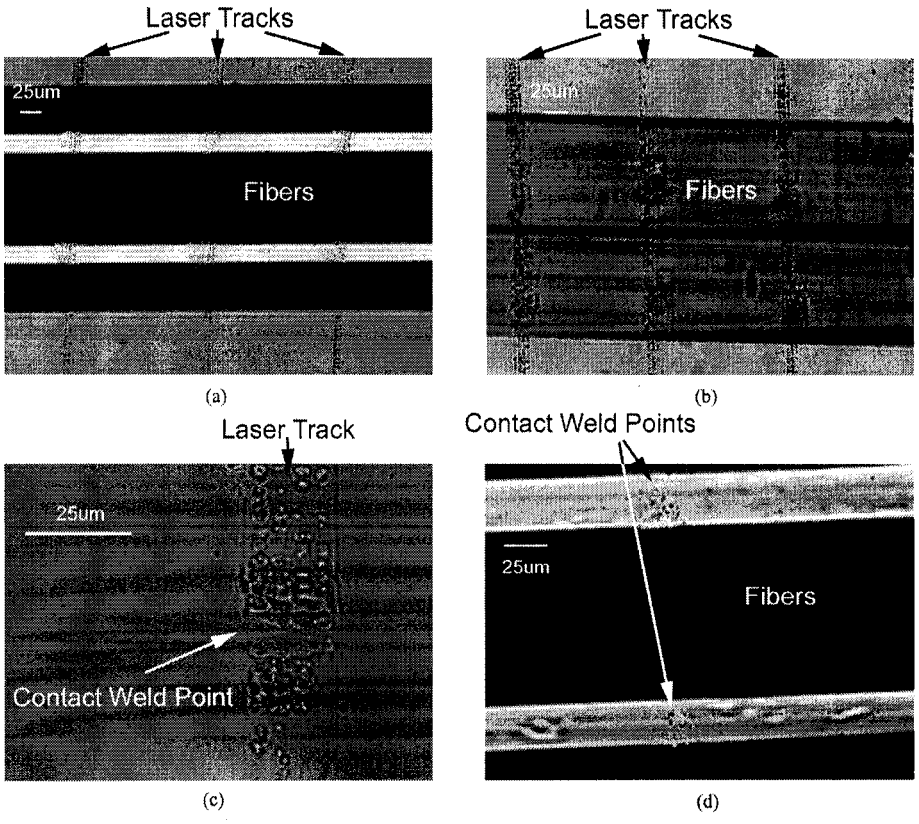

Figure 4.1: Optical microscope images of the welded optical fibers on a fused silica coverslip. 20x magnified images of back surface welding lines and contact points imaged from (a) the fiber side and (b) the fused silica side. (c) 100x magnified image of back surface welding lines and contact points imaged after the optical fiber was pulled off from the fused silica coverslip. (d) 40x magnified image of the optical fiber surfaces after they were pulled off.

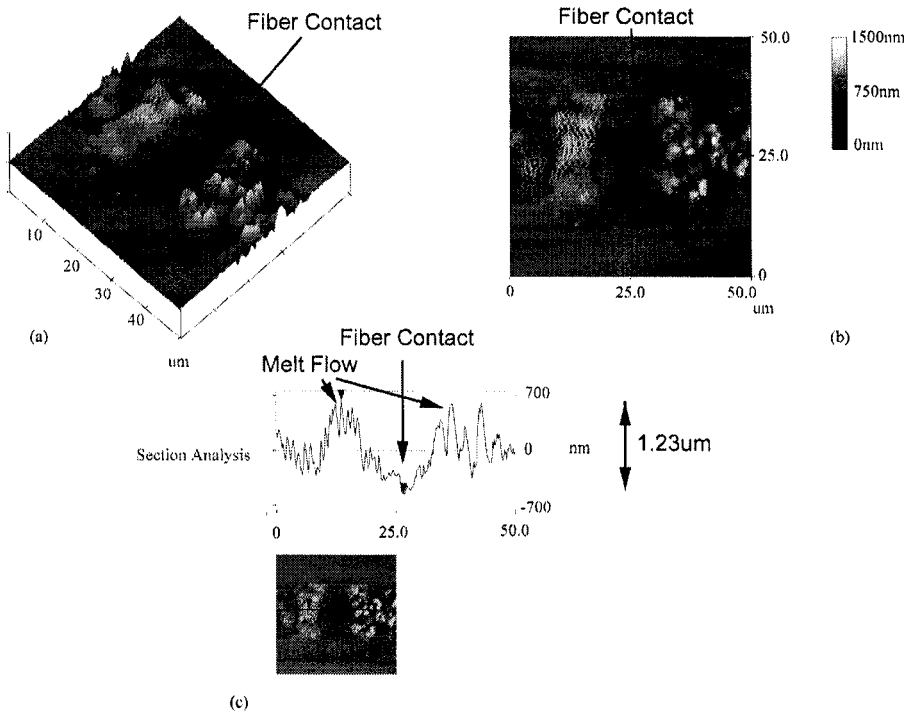

Figure 4.2: AFM images of the welding contact points on the fused silica coverslip surface after fiber was pulled off in different views: (a) 3-dimensional view, (b) top view and (c) cross-sectional view. The cross-sectional view showed the melted glass re-solidified and conformed to the shape of the optical fiber.

The melted glass had a vertical height of 1.3 to 1.4 μm as shown in Figure 4.2c. The images in Figure 4.2 show the melted glass from the fused silica slip and optical fiber conformed to the shape of the optical fiber and re-solidified to form a weld contact.

4.1.2 Discussion

The F_2 welding of glass optical fibers onto fused silica slips was the preliminary work to demonstrate the potential application of the F_2 laser in welding of transparent glasses. As shown in Figure 4.1 and Figure 4.2, the weld contact points were formed from the melted glass due to the laser energy deposited at the interface between the fiber and fused

silica coverslip. There is only a narrow fluence range of ~2.61 J/cm^2 to ~3.66 J/cm^2 in which the focused laser beam is able to melt the glass at the back surface without pronounce ablation or front surface ablation. As the fluence increases up to 2.08 J/cm^2, no effect is seen on either substrates until the fluence is strong enough to melt the glasses on the back surface. Back surface ablation occurs above 2.08 J/cm^2 and eventually front surface ablation is observed at single-pulse fluence above 4.07 J/cm^2. The observations were summarized in Table 4.1.

The reason for this narrow welding window is the onset of front surface ablation which redirects absorption from the back surface to the front surface. Although the fused silica is of UV grade, a test revealed a transmission of ~56% with a thickness of 160 μm. The absorption poses the issue that a single-pulse fluence of 2.08 J/cm^2 to 3.81 J/cm^2 measured at the nozzle is required for the back surface to melt or ablate. With the high single-pulse fluence, the front surface is near its ablation threshold and a slight raise of energy will initiate front surface ablation. The upper limit is caped under a single-pulse fluence of ~3.66 J/cm^2. The lower limit is imposed by the onset of melting and pre-ablation on the back surface with a single-pulse flunce of more than 2.6 J/cm^2. A distinct melted laser track is defined as the melting onset and provides the weld spots. Hence, a narrow fluence range of 2.61 J/cm^2 to 3.66 J/cm^2 for a focal spot size of 25 μm x 25 μm can provide a transmission welding through fused silica coverslip with an optical fiber.

The laser melted glass resolidified, as can be observed from Figure 4.1 and Figure 4.2, conformed to the shape of the optical fiber. The contact weld points produced an average reflow height of ~1.3 to 1.4 μm which was approximately $\frac{1}{100}$ of the fiber diameter and covered ~4% of the welded fiber circumference. It is possible that the molten glass was ejected from the fused silica coverslip and mixed with the molten glass on the fused silica-optical fiber interface. This can be inferred from the evidence provided from the high volume of glass wrapping around the fiber.

Furthermore, the silica SMF-28 optical fiber is highly absorbing at a wavelength of 157 nm compared to the UV grade fused silica coverslip. This offers higher heating efficiency of the fiber surface. And the close contact between the two surfaces provides a conduction path for heat transfer causing a melt phase on both surfaces contribute to the weld. Hence, ten welded spots were able to hold the a 3cm long optical fiber.

Further study is required on F_2-laser welding to assess the strength of the welding spot. Another step is to attempt to weld two pieces of glass together. This will allow a true single step integration of a glass biophotonics lab-on-a-chip with optical circuits, microfluidic channels, and sealing coverslips.

4.2 Ge-doped FHD Silica Optical Circuits

4.2.1 Waveguide Characterizations

Ge-doped FHD silica optical circuits were fabricated and first tested with 4 μm wide straight waveguides. As noted in Section 3.2.1.1, the waveguides were designed to be single mode at the wavelength of 632.8 nm. The exposure conditions are summarized in Table 4.2. Three FHD with Ge-doped concentration 3%, 7% and 10% were tested. The corresponding type of waveguide, net fluence, single-pulse fluence, exposure time and waveguiding of red light at 632.8 nm are listed.

For the three FHD samples tested, only Sample A with the highest Ge content of 10 wt% had no evidence of refractive index modification and densification. Refractive index contrast under a differential interference contrast (DIC) microscope and guiding of light at 632.8 nm were not observed.

Both sample B and C were able to guide light and a DIC microscope image of Sample C is shown in Figure 4.3a providing the evidence of refractive index modification. Moreover, the interface between the FHD germanosilicate and the pure silica oxide, which is $\sim$2 μm deep from the surface, had a visible strip as seen in Figure 4.3b.

Table 4.2: This table summarizes the Ge-doped FHD waveguide results.

Sample	A	B	C	D
Waveguide Type	Straight	Straight	Straight	Y-Branch
Ge Content (weight)	10%	7%	3%	3%
Total Fluence (kJ/cm^2)	27.5	33.6	65.3	68.9
Fluence per Pulse (mJ/cm^2)	13.3	16.8	19.0	20.5
Exposure Time	5hrs	5hrs	8hrs	8hrs
Waveguiding	NO	YES	YES	YES

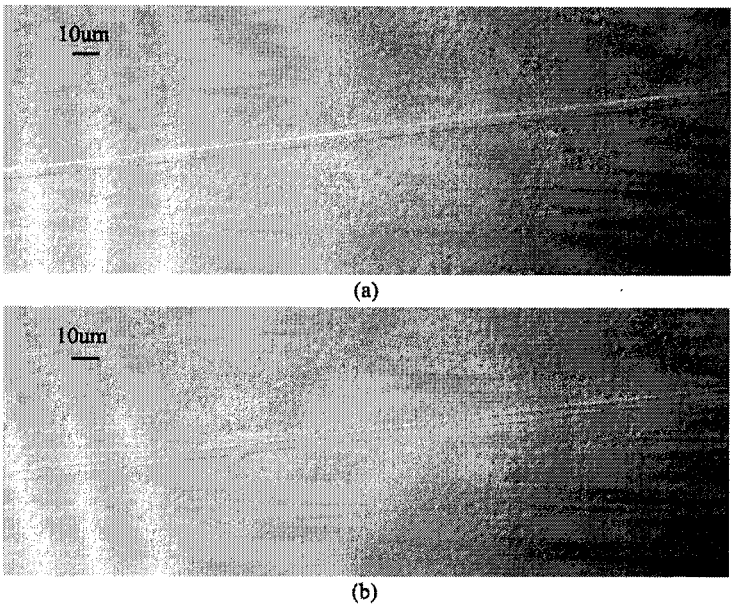

Figure 4.3: DIC microscope images of a planar straight waveguide (Sample C) with a width of 4 μm and a height of 2 μm imaged (a) on the surface to show the refractive index modified area and (b) $\sim$2 μm below the surface which was believed to be the interface between the FHD germanosilicate and the pure silica oxide.

The guiding of HeNe laser light at 632.8 nm was achieved by an input coupling 40x objective lens (N.A = 0.65). A 20x objective lens (N.A = 0.40) was used to collect the output light. The image in Figure 4.4 shows the near field mode profile output from

Sample C.

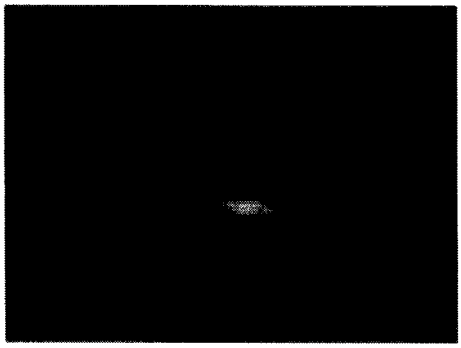

Figure 4.4: An image of the near field mode profile of a planar straight waveguide (Sample C) excited by a HeNe laser (632.8 nm).

A high Ge content (10 wt%) highly absorbs the 157 nm radiation and refractive index contrast was not observed under the DIC microscope. For lower Ge content (7 wt% and 3 wt%), apparent change of refractive index was observed.

4.2.2 Y-Branch Characterizations

The straight waveguide results of Section 4.2.1 were designed to test the optimum composition of Ge content. Evidence of refractive index modification by 157 nm irradiation in lower Ge content (7 wt% and 3 wt%) FHD silica samples helped to decide the suitable composition for Y-branches fabrication. A 3 wt% Ge-doped FHD silica sample was chosen due to its pronounced photosensitivity and a lower 157 nm absorption due to low Ge content.

The exposure conditions for creating Y-branches are summarized in Table 4.2. The corresponding type of waveguide, net fluence, single-pulse fluence, exposure time, and waveguiding in 632.8 nm are listed.

Comparing to the previously written waveguides, a higher net fluence of 68.9 J/cm^2 was used to ensure that a refractive index modification would be induced. For all the

samples fabricated, no photosensitization by hydrogen loading was required or performed. A DIC microscope image is shown in Figure 4.5 for one of the Y-branches fabricated.

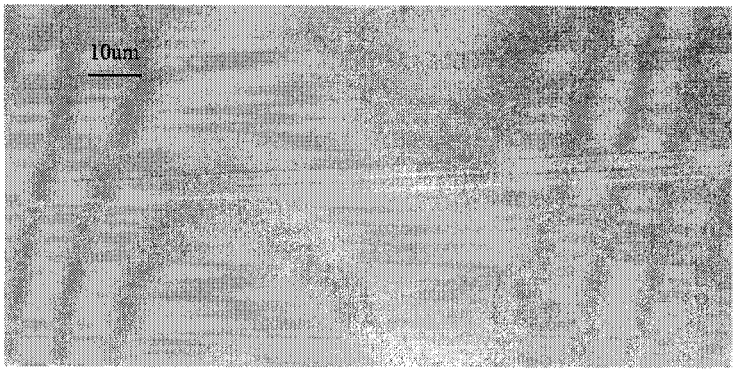

Figure 4.5: A DIC microscope image of a symmetric Y-branch after the irradiation with F_2 laser. The width of the waveguide and the branches are 4 μm and 2 μm, respectively. The depth of the waveguide and branches is 2 μm.

A HeNe laser(632.8 nm) was used for the input. An image of the mode profiles from one of the asymmetric waveguides is shown in Figure 4.6.

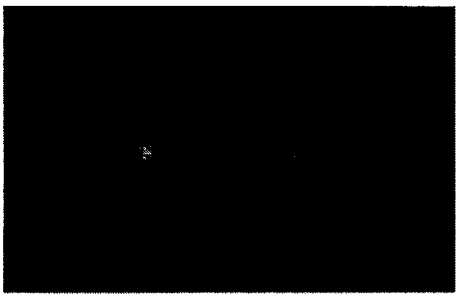

Figure 4.6: An image of the near field mode profile of a asymmetric Y-branch with a HeNe laser (632.8 nm).

Non-uniformities in the energy distribution were observed under the microscope for the fabricated Y-branches. This distortion is possibly due to uneven laser exposure of the Y-branches at different positions. The top portion of the exposed area had the highest dosage. Therefore, the top Y-branch received the highest dosage giving rise to the highest

refractive index change.

In coupling HeNe laser (632.8 nm) in the top symmetric Y-branch, multi-mode guiding was observed. Moreover, the densification variation observed under the optical microscope provided a qualitative assessment that the top area received higher net fluence. Although single mode was desired, the multi-mode Y-branch indicated the upper limit of the irradiation dose for refractive index change for single mode. Using a 2-dimensional BPM software (Optiwave), an estimation of the refractive index change in order for a 2 μm wide and deep waveguide to become multi-mode was calculated to be $3.7\text{x}10^{-3}$.

4.2.3 Discussion

From the results presented in Section 4.2.1 for straight channel waveguides, Sample C containing the highest Ge content (10%) yielded no evidence of densification or refractive index change. This is due to a Ge content exceeding the threshold where this highly absorbing material prevents sufficient penetration depth for refractive index modification to guide light. The maximum Ge content for this to occur requires further experimental work. However, it is clear that the threshold lies between a Ge content of 7% and 10% since Sample B (7 wt%) shows evidence of red light guiding and densification.

For the channel waveguide written in Sample C with a Ge content of 3%, a noticeable channel strip can be observed under a DIC microscope as seen in Figure 4.3b. This strip is believed to be at the interface between the FHD germanosilicate layer and the silica oxide. This interface defines the depth of the channel waveguide due to the more than ten fold decrease of photosensitivity from the absence of Ge in the silica oxide as suggested in [107, 108]. Moreover, the absence of hydrogen loading photosensitization provides a more rapid method for prototyping and designing of waveguide circuits.

The Y-branches fabricated on Sample D yielded a variation in the amount of refractive index modification in the vertical direction on the irradiated area. This is due to the cyclindrical lens that focused the laser beam onto the NiCr-masked FHD sample to

create a non-uniform horizontal beam. The center of the beam was higher in fluence and the fluence dropped off vertically from the center toward the top and bottom. A simple experiment on PMMA ablation was performed to verify this nonuniformity. A higher ablation depth was noticed in the center of the beam area and the ablation depth gradually fell off from the center. The setup as shown in Figures 3.6 and 3.7 was placed in the first section of the laser processing chamber without the homogenization optics. Hence, the raw laser beam from the F_2 laser was directly focused onto the sample through the cylindrical lens and an aperture to represent the beam profile used to expose the FHD samples.

For future work, the primary goal should be to homogenize the laser beam for uniform irradiation of the NiCr-masked FHD sample. The fabrication setup should be placed after the homogenization optics which produces a 5 mm x 5 mm uniform beam. However, the available space in the processing chamber prevent the existing setup to be placed elsewhere other than the present location. Therefore, a new and more compact design for the setup is required.

Refractive index characterization is also another factor that needs to be considered in the future work. The estimated refractive index contrast of $3.7\text{x}10^{-3}$ for a 2 μm wide and deep waveguide with a net fluence of 71.6 kJ/cm^2 is very crude since a 2D BPM software (Optiwave) was used to find the minimum index increase required for a two-moded guiding for the designed waveguide at 632.8 nm. Other methods including near field modal profiling and microreflectivity [109] for determining the refractive index profile of the written waveguides can be employed.

4.3 F_2 Buried Waveguide Characterizations

4.3.1 Near Field Modal Profiles

The near field modal profiles were captured with a CCD with a 100x microscope objective lens having a N.A of 0.95 as discussed in Section 3.3.1. The F_2 waveguide profiles had an elongated shape in the F_2-laser irradiated direction. The width of the waveguides was defined by the width of the squares on the aluminum amplitude mask which was demagnified to 6 μm. Buried waveguides with depths of 10 μm to 25 μm from the surface were fabricated by focusing the image of the square array inside the bulk fused silica glass on a computer controlled *xyz* translation stage. Figure 4.7 shows the buried waveguides with depths of ~10 μm and ~15 μm measured from the sample surface. The depth of the waveguides were measured from the surface of the sample to the middle of the near field modal profile as shown in Figure 4.7.

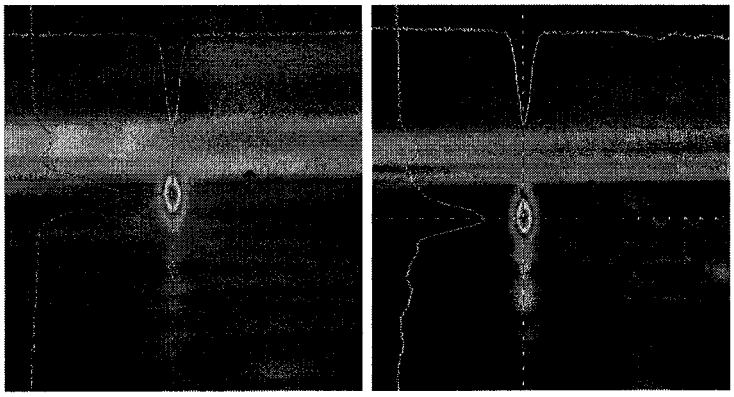

Figure 4.7: Near field modal profiles showing the depth of the buried waveguides: (a) ~10 μm and (b) ~15 μm from the edge of the bulk fused silica.

The near field modal profiles captured in Figure 4.8 were for waveguides receiving a net fluence of ~20 kJ/cm^2 written with a scan speed of 0.65 μ/s. The elongated mode was apparent in the laser irradiated direction. The mode shape remained closely related to the square width in the transverse direction. Several modal profiles are shown in

Figures 4.8 and 4.9 in 635 nm and 1550 nm, respectively.

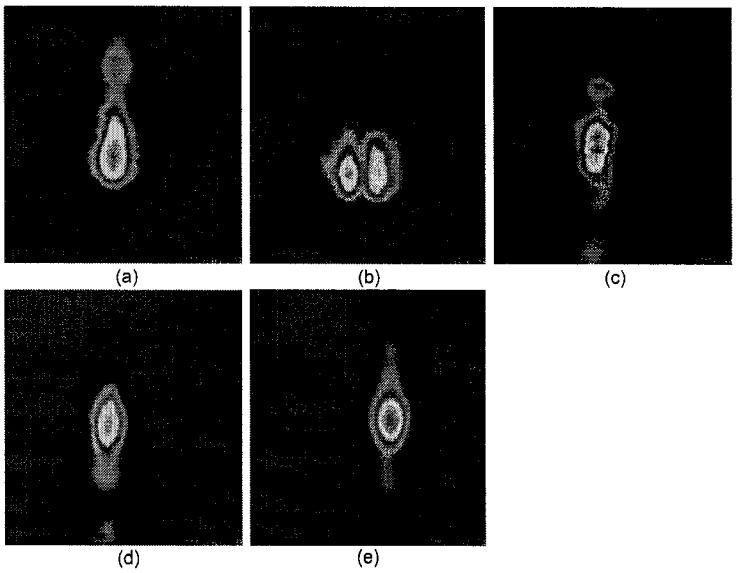

Figure 4.8: Near field modal profiles of F_2 buried waveguides with a net fluence of 20 kJ/cm^2 and depths of (a),(b) 10 μm, (c) 15 μm, (d) 20 μm, and (e) 25 μm in red (635 nm). Near field modal profiles of 10 μm deep waveguide showing (a) single-mode and (b) multi-mode in red (635 nm).

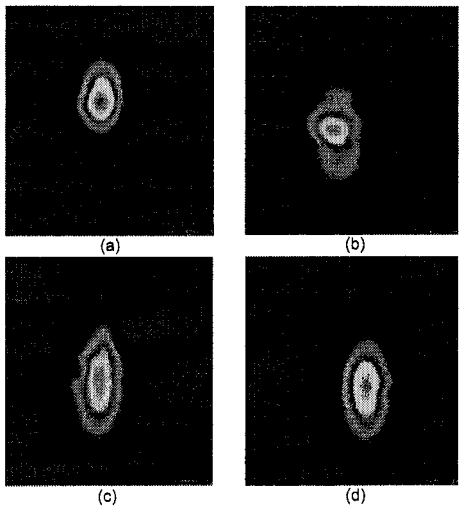

Figure 4.9: Near field modal profiles of F_2 buried waveguides with a net fluence of 20 kJ/cm^2 and depths of (a) 10 μm, (b) 15 μm, (c) 20 μm, and (d) 25 μm in IR (1550 nm).

The $\frac{1}{e^2}$ intensity distance of both the red and IR modes were determined by the Spiricon software. With a net fluence of ~20 kJ/cm^2, the refractive index change was high enough to observe multi-mode formation in red light as reported in [109]. The transverse modal width for the waveguides ranged from 10.3 μm to 15.2 μm in red and 15.4 μm to 16.8 μm in IR. The depth of these waveguides ranged from 10 μm to 25 μm.

4.3.2 Insertion Loss

The insertion losses of the F_2 buried waveguides were measured using the methods described in section 3.3.2. A reference was first obtained by direct fiber-to-fiber coupling. The insertion loss for each waveguide was obtained from the difference between the reference and the waveguide transmission spectrum from fiber butt coupling. Figure 4.10 and Figure 4.11 show the reference spectrum, waveguide transmission spectrum, and difference between the spectrums in infrared and red, respectively.

A large portion of the insertion loss of ~12 dB was due to the coupling loss from the bevel on the input and output facets even with the aid of refractive index matching fluid. The graph in Figure 4.12 summarizes the insertion loss for waveguides having depths from ~10 μm to 25 μm both in red and IR.

For these near surface buried waveguides, insertion losses were later used for references to extract scattering and reflection losses due to microfluidic channels.

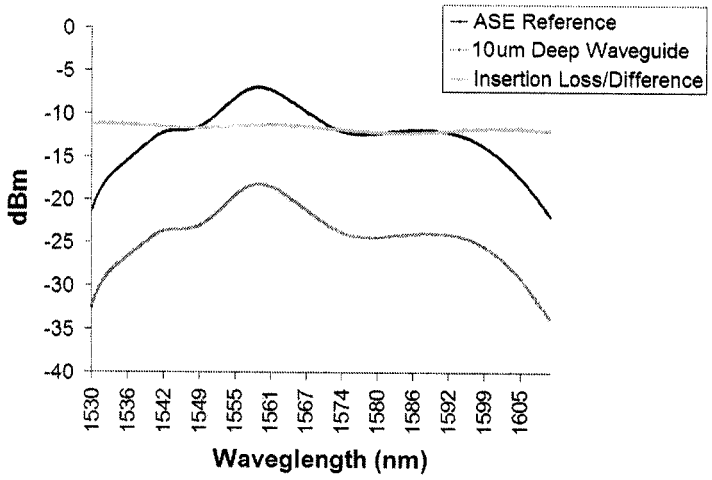

Figure 4.10: The transmission insertion loss of the F_2 buried waveguide in IR. The output transmission spectrum from fiber butt coupling of the waveguide is compared with the reference from direct fiber-to-fiber coupling. Both the transmission spectrum and insertion loss are obtained.

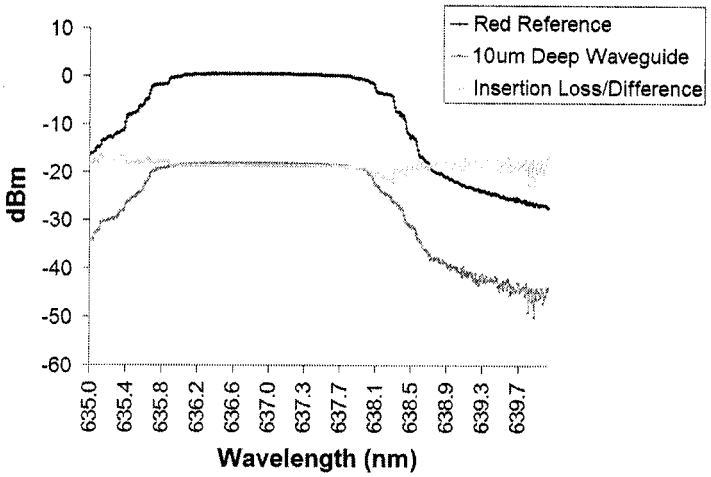

Figure 4.11: The transmission insertion loss of the F_2 buried waveguide in red. The output transmission spectrum from fiber butt coupling of the waveguide is compared with the reference from direct fiber-to-fiber coupling. Both the transmission spectrum and insertion loss are obtained.

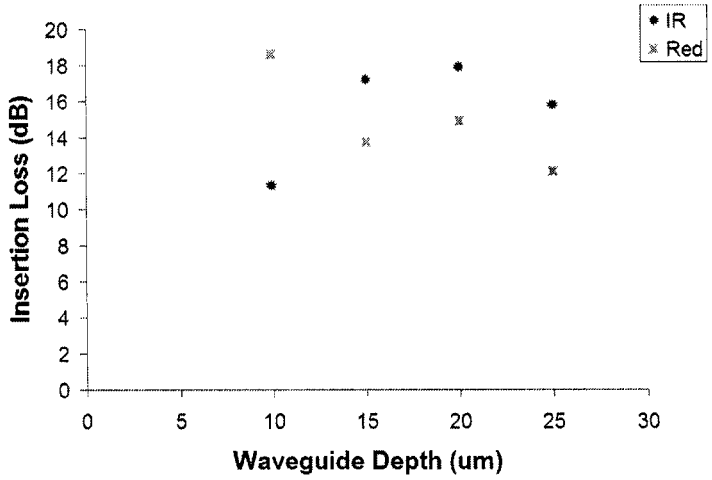

Figure 4.12: A graph of insertion loss versus F_2 buried waveguide depth. The high insertion losses are possibly due to the rough input and output facets from the bevel and the high propagation loss of the waveguide.

4.3.3 Propagation Loss

The propagation loss was measured with a CCD camera (Panasonic GP-KR222) above the F_2 waveguide sample. The method in Section 3.3.3 was used to measure the loss due to scattering light which provided an estimation of the propagation loss. A red light source (635 nm, Thorlabs Inc. S1FC63S) was used for input. An image captured for measurement of the waveguide propagation loss is shown in Figure 4.13.

The F_2 buried waveguides written with a designed depth of 10, 15 and 20 μm had propagation loss values of 13.5, 3.6 and 6.7 dB/cm, respectively. Figure 4.14 shows a semi-log plot of the scattered light intensity plotted along a 0.5 cm long segment of waveguide. The slopes of the data yield a loss estimate of the fabricated waveguides.

Figure 4.13: A CCD captured gray-scale image illustrating the exponential decrease of the scattering power (right to left) due to propagation loss at a wavelength of 635 nm.

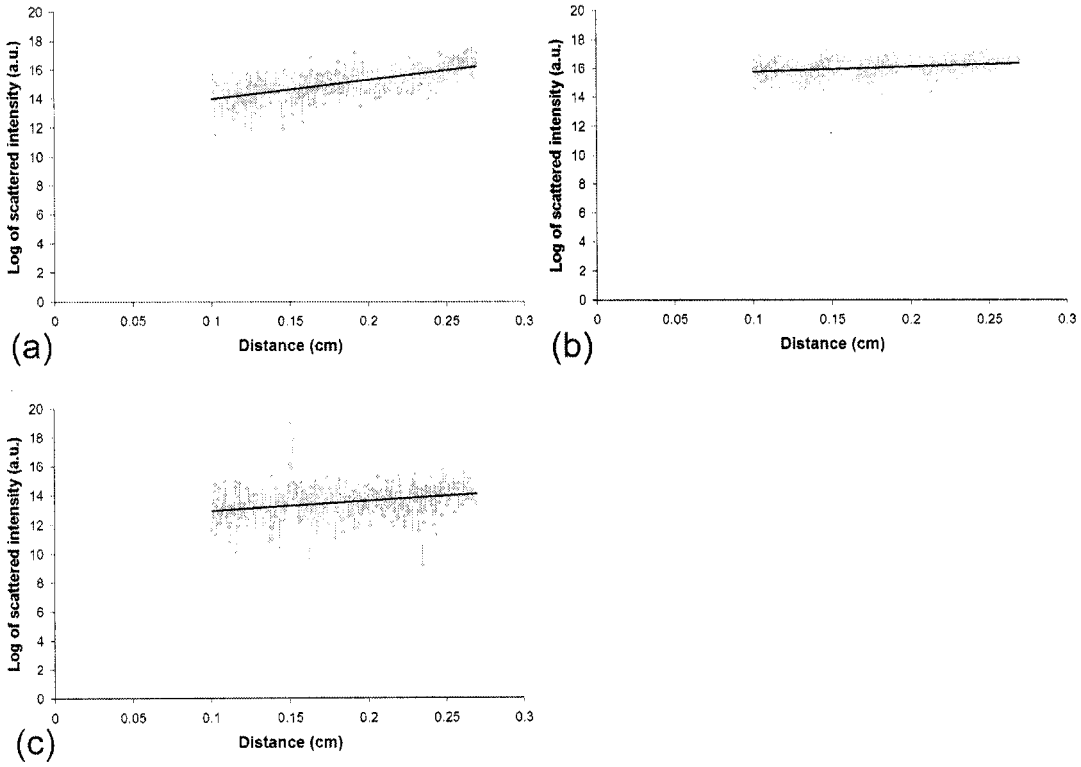

Figure 4.14: Log of scattered intensity as a function of the distance from the end facet for waveguides formed at depths of (a) 10 μm, (b) 15 μm, and (c) 20 μm in bulk fused silica. The slope of the least squares fit of the data (solid lines) provides a propagation loss estimate of 13.5 dB/cm, 3.6 dB/cm, and 6.7 dB/cm, respectively.

4.3.4 Refractive Index Determination

The $\frac{1}{e^2}$ distances of the near field modal profiles were used to estimate the maximum refractive index change of the F_2-laser formed buried waveguides with depth from 10 μm to 25 μm. RSoft method of Section 3.3.4 was used to determine the corresponding modal profiles by varying the refractive index contrast. Hence, the peak refractive index change could be found.

With a step-index cylindrical waveguide simulation with a diameter of 6 μm, refractive index contrast for both red (635 nm) and infrared (1550 nm) were obtained. For the red, refractive index contrast of $5.5\text{x}10^{-4}$ to $8.2\text{x}10^{-4}$ for transverse near-field mode distance ($\frac{1}{e^2}$) of 15.2 to 10.3 μm was calculated from the simulation. For the infrared, refractive index contrast of $3.1\text{x}10^{-3}$ to $3.3\text{x}10^{-3}$ for near-field mode distance ($\frac{1}{e^2}$) of 15.4 to 16.8 μm was calculated. These refractive index contrast values were close to the results for F_2 buried waveguides with a net fluence of 20 kJ/cm^2 acquired previous by Valdivia et al. using microreflectivity [109].

4.3.5 Discussion

F_2 laser fabricated buried waveguides for guiding of visible and infrared light were previously demonstrated by Herman and coworkers [49,65,109]. The present results for near field modal profile, insertion loss, propagation loss and refractive index contrast extend this previous data to waveguides which are formed at 10 μm to 20 μm from the surface of the fused silica block. Previous work in Herman et al. was focused on waveguides buried at a depth of >50 μm.

The near-field modal profiles observed were elongated in the vertical direction (parallel to the laser irradiation direction) compared to the transverse direction (perpendicular to the laser irradiation direction) as seen in Figures 4.8 and 4.9. This is due to a large depth-of-focus (DOF) of the laser beam focusing an image of a 6 μm x 6 μm square with

the Schwarzchild lens (N.A.=0.4) and the DOF is approximately 10 μm (by geometrical approximation). Moreover, the refractive index contrast in the irradiated direction was not a step-index profile due to the variation of the laser energy as it became focused and de-focused in the bulk fused silica glass.

An improvement in the measurement of near-field modal profiles could be achieved by using larger lenses for focusing. This allows more pixels to be filled on the CCD camera leaving less noise being measured for the determination of near-field modal widths with the Spiricon software. With the present setup, a signal fluctuation of the near-field modal width determination up to 0.1 μm was observed due to the noise level on the CCD camera. The transverse modal widths are 15.2±0.1 μm to 10.3±0.1 μm and 15.4±0.1 μm to 16.8±0.1 μm in red (635 nm) and infrared (1550 nm), respectively.

The results for insertion loss showed that there might be dependence on waveguide depths. As shown in Figure 4.12, one can observe the insertion loss for the infrared guiding waveguides increases as the depth increases until the depth reaches 25 μm. This is also observed in the red except the 10 μm deep waveguide has the highest insertion loss which is due to high propagation loss as shown in Figure 4.14. The insertion loss dependence on waveguide depths requires further investigation. However, the reduction of insertion loss for the 25 μm deep waveguide was probably due to the absence of bevel edges on one, or both, end facets due to the waveguide depth.

As discussed in the previous paragraph, the propagation loss varies for various waveguide depths from 10 to 20 μm. Although the method employed for finding the propagation loss is convenient and provides a quick estimate on the loss from the scattered light , the scattering centers as observed in Figure 4.13 fluctuate from pixel-to-pixel. The scattering centers were not very prominent and hence, the propagation loss measurements were well represented by an exponential fit. Another common method for propagation measurement is the cut-back technique. Although it was not employed in this work, it would offer further verification of the propagation loss. One drawback is that it requires

a large sample for dicing into various sizes, and a consistent quality of high polishing for similar low insertion loss for every piece. For the samples fabricated, the bulk fused silica block of 5 mm x 5 mm x 10 mm was too small for the cut-back method.

The refractive index contrast values determined through a fitting process using the RSoft simulation package of Section 4.3.4 have inaccuracies. Firstly, the refractive index modification zone did not have a step-index profile which was used for simulation purpose. Secondly, the waveguides might not be 6 μm in width. For the latter issue, BPM simulations were performed to understand the effect of the waveguide widths toward the variations in near-field modal width for their corresponding refractive index contrast values. The results were plotted as a series of waveguide widths with $\frac{1}{e^2}$ near-field modal width (intensity) as a function of refractive index contrast values in both infrared (Figure 4.15) and red (Figure 4.16).

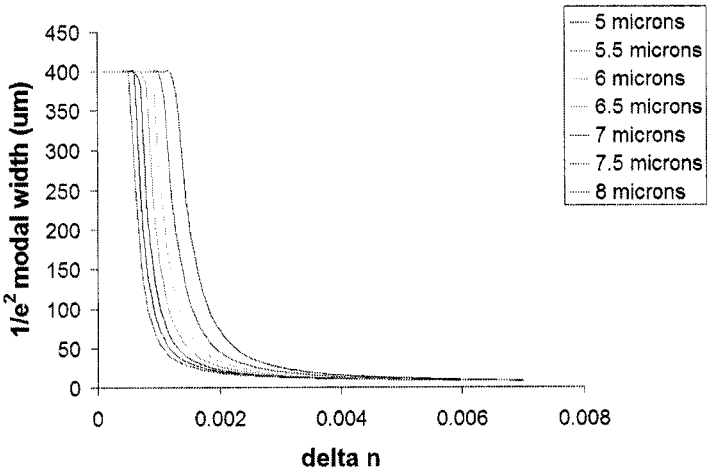

Figure 4.15: RSoft CAD simulation results for various waveguide widths and the respective $\frac{1}{e^2}$ modal width for different refractive index contrast values were plotted. The simulations were done with a step-index profile at a wavelength of 1550 nm and a substrate background index of 1.444 for UV-grade fused silica.

For the results in both infrared and red, the uncertainty of ± 0.10 μm for the near-

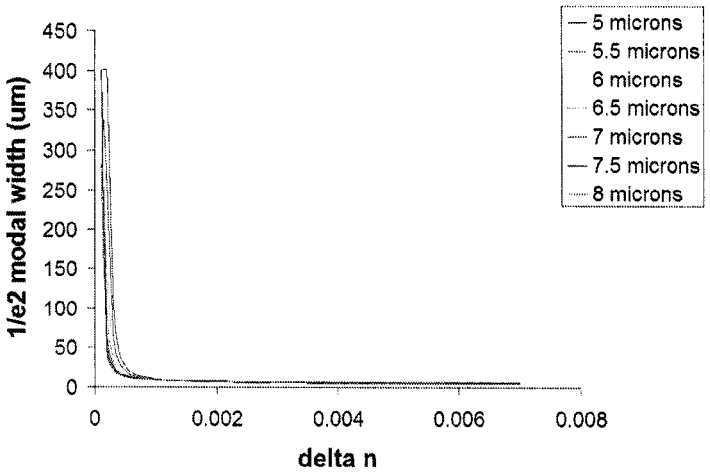

Figure 4.16: RSoft CAD Simulation results for various waveguide widths and the respective $\frac{1}{e^2}$ modal width for different refractive index contrast values were plotted. The simulations were done with a step-index profile at a wavelength of 635 nm and a substrate background index of 1.457 for UV-grade fused silica.

field modal width measurement mentioned previously correspond to <0.0001 (<3% for infrared and <10% for red) refractive index difference for a 6 μm wide waveguide. For waveguide core width of ± 1 μm measurement error (waveguide widths ranging from 5 μm to 7 μm), the refractive index contrast values have a difference of approximately 0.0007 (approx. 24%) in infrared and 0.0001 (approx. 10%) in red to achieve the measured near-field modal width. The mode widths for different waveguide core widths begin to converge at refractive index contrast values of ~0.005 for infrared and ~0.001 for red. Any values lower than these result in a significant change of mode widths for a small change in refractive index contrast values. Other methods of refractive index contrast determination are required for more accurate measurements. Microreflectivity techniques have been proven to be a more reliable method as was previously employed by Herman and coworkers [109].

The reflective index modification mechanisms were not studied here. However, the

color-center model and the densification model are expected to play a role. However, in the case of F_2 laser induced refractive index modification, the color-center model is not the dominant mechanism. This model follows the Kramers-Kronig relationship (Equation 2.3) which states that the photoinduced changes in the absorption spectrum give rise to the refractive index change [41] and the equation shows that a higher refractive index change should occur for a wavelength that's closer to the resonant wavelength and decrease as it is further away. In the case of F_2 waveguides, it is shown that the refractive index contrast values are higher in infrared than in red which is the inverse of what should be expected from the color-center model. Therefore, another mechanism or the densification model may be in play and dominating the role of refractive index modification.

Although the previous explanation is a plausible reason for the inverted level of index contrast values for red and infrared, another reason could be the uncertainty in determination of the near field modal profiles for the red. As mentioned previously, the waveguides fabricated with a net fluence of 20 kJ/cm^2 begin to display higher order modes. Since the refractive index contrast values were determined from the fundamental mode, the modes measured for red might not be the tightest modes which correspond to the fundamental modes. With a larger mode width, a reduced index contrast value is obtained. Hence, this can help to explain the discrepancy. For the infrared modes, the waveguides were single-mode and the uncertainty in the measurement did not affect this discrepancy.

Chapter 5

F_2-Laser Microfabricated Biophotonics Device

In the previous chapter, the building blocks essential for creating a biophotonic lab-on-a-chip was presented. In this chapter, the results of a F_2-laser fabricated device with a buried waveguide intersecting a microfluidic channel are presented. As previous work with refractive index modification in fused silica employing F_2-laser showed successful optical waveguide writing, a microfluidic channel was subsequently ablated perpendicular to the waveguide. The result is a device which can detect particles crossing the intersection between the waveguide and the micro-channel. The waveguide probes the particle inside the channel and the micro-channel represents a basic component for fluid and particle transport. This simple device proves the potential success of F_2-laser single step integration of optical capabilities onto microfluidic structures in glass.

5.1 Waveguide Integrated with Microfluidic Channel

5.1.1 Insertion Loss

The added optical insertion loss due to the formation of an intersecting micro-channel was measured by both methods in Section 3.3.2 for comparison purposes. The separation formed by the micro-channel generated loss due to scattering, Fresnel loss, beam divergence, and beam deflection at the interface of the waveguide and the micro-channel. Figure 5.1 shows a CCD image of a red light (635 nm) in the waveguide horizontally intersecting a micro-channel.

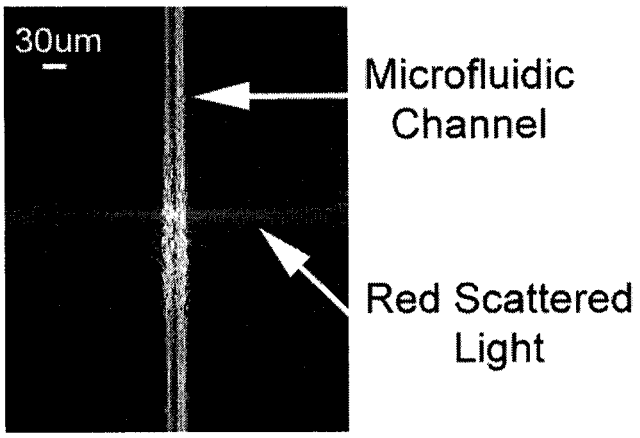

Figure 5.1: A red (635 nm) guiding waveguide intersecting a micro-channel. Scattering and reflection of the light from the micro-channel surfaces could be seen.

This additional loss was obtained by comparing the insertion loss measurement obtained for the F_2-laser formed waveguides before and after the ablation of the micro-channels. Table 5.1 shows the insertion loss results with only air in the micro-channels.

With distilled water flowing through the micro-channels, the optical loss was reduced due to lowered refractive index contrast between the fused silica waveguide and the water-filled micro-channel. Table 5.2 lists the loss reduction due to addition of water in the micro-channels.

Table 5.1: Insertion loss of optical waveguides with air-filled micro-channel.

Waveguide Depth from Surface	Wavelength (nm)	Waveguide Only (dB)	Waveguide + Channel (dB)	Micro-channel Loss (dB)
10 μm	635	-18.6	-26.8	8.2
10 μm	1550	-11.3	-26.1	14.8
15 μm	635	-13.7	-23.0	9.2
15 μm	1550	-17.2	-26.5	9.2

Table 5.2: Insertion loss of optical waveguides with air-filled micro-channel and water-filled micro-channel.

Depth from Surface	Wavelength (nm)	Waveguide + Dry Channel (dB)	Waveguide + Wet Channel (dB)	Reduced Loss (dB)
10 μm	635	-26.8	-25.1	1.7
10 μm	1550	-26.1	-24.2	1.9
15 μm	635	-23.0	-21.0	1.9
15 μm	1550	-26.5	-23.1	3.3

5.1.2 Microsphere Detection

Microspheres were flowed through the micro-channel for testing the detection sensitivity of the device. The device had a 10 μm deep optical waveguide, and a 30 μm wide and 35 μm deep micro-channel. The micro-channel depth was designed to ensure the pre-existing waveguide was intersected and hence, the waveguide could be used to interrogate the contents inside the micro-channel. The micro-channel depth was set to be 35 μm because of the reasons explained in section 3.2.3.2.1, namely, the optimum depth for producing a steep and smooth wall with nearly micro-crack free edges.

The diagnostic arrangements described in section 3.3.4 were used to detect microsphere. The first method (ASE source + OSA) provided an accurate reading of a static microsphere positioned in the micro-channel intercepting the path of the intersecting waveguide. Table 5.3 summarizes the results for static detection of a microsphere and the resultant signal drop. The signal drop due to the microsphere was weaker in IR than in red as observed in the Table 5.3.

Table 5.3: Insertion loss of optical waveguide with water-filled micro-channel and a static microsphere in the micro-channel.

Depth from Surface	Wavelength (nm)	Waveguide + Wet Channel (dB)	Waveguide + Sphere in Channel (dB)	Signal Drop (dB)
10 μm	635	-25.1	-27.5	2.4
10 μm	1550	-24.2	-24.6	0.4

However, a microsphere would not remain static at one position. Therefore, the second method (laser + optical detector + optical power meter) was used to provide a more dynamic and meaningful reading of the detected signal. Figure 5.2 shows the signal reduction due to the crossing of microspheres at two different time intervals.

The data points were captured at a frequency of 200 Hz and the input source was a red laser (635 nm). The signal drop due to the microspheres ranged from ~0.13 dB to 0.14 dB.

For dynamic microsphere detection, a weaker signal contrast was noted in both red and IR. The IR signal contrast was too weak to be distinguished from the noise signal due to the transparent microspheres in IR and a very faint signal drop was detected. The microsphere had a higher absorption of red light. Hence, red light was favored for microsphere detection for both the static and the dynamic microspheres cases.

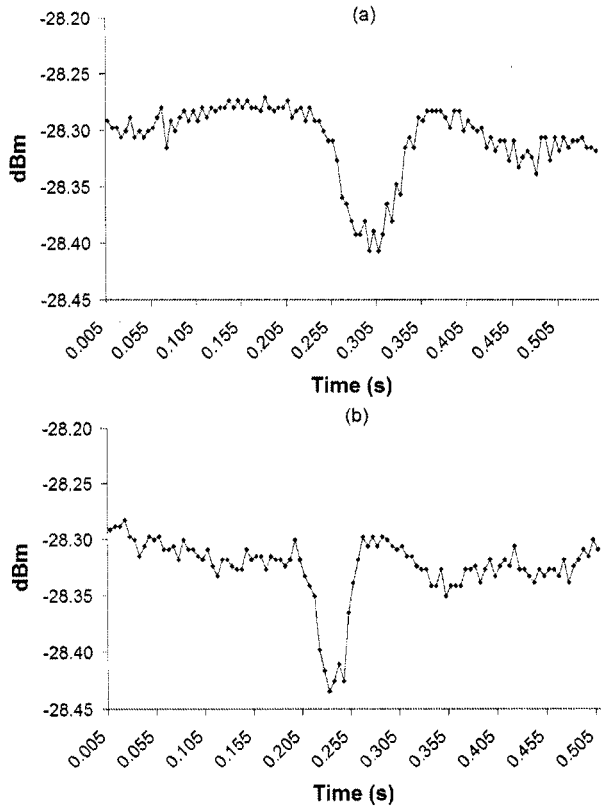

Figure 5.2: A plot of power (dBm) versus time (s) when two microspheres flowed through the micro-channel intersecting a waveguide. Red (635 nm) laser was used for the input source and a power detector connected to a power meter was used to detect the spheres, namely (a) 1st microsphere and (b) 2nd microsphere.

5.2 Discussion

This work is focused on detecting particles flowing through a 30 μm wide micro-channel which performs as a basic cytometer. Polystyrene microspheres with a diameter of $\sim$15 μm were used for simplicity. The buried waveguides fabricated with the F_2 laser had a total insertion loss between -13 dB to -19 dB in red with the help of refractive index matching fluid. After accounting for the propagation losses, the -13 dB to -19 dB losses were reduced to $\sim$12 dB for waveguides 10 μm and 15 μm deep. The large range was

probably due to the uneven roughness on the bevel edges of the bulk fused silica. This loss could be improved by polishing the input and output facets to remove the bevels.

The data of Table 5.1 shows that the formation of a micro-channel intersecting the waveguides caused an additional loss of 8 dB to 15 dB. The loss included the light divergence from the disconnected waveguides due to the micro-channel gap (~35% or ~1.9 dB), the reflection loss of ~0.32 dB due to the refractive index contrast (two interfaces of glass to air), beam deflection loss due to the slanted channel wall (~11°) of ~2.2 dB, mode mismatch loss of fiber to laser formed waveguides (~2 to 4 dB) and scattering loss from the two interfaces which accounts for rest of the insertion loss(glass-to-air and air-to-glass from the intersecting micro-channel).

To improve on the loss, ablation at higher fluence is required to provide smoother and more vertical walls. The maximum fluence the F_2 laser can deliver currently is in the range of 4 to 5 J/cm^2. The best results were obtained when the laser was operating at its optimal condition generating a fluence of 9 J/cm^2 [83] and higher fluences may be ideal.

Another factor concerning the fluence level is the laboratory humidity. A fluctuation of the humidity correlates to the amount of time for out-gasing and dehumidifying of the laser processing chamber. With humidity of more than 50%, a purging time of at least 5-6 hours is required to clear the optics and chamber of air and excess moisture whereas a typical time of 2-3 hours is required for a humidity of 45%. The moisture on the optics and oxygen absorbs the 157 nm light strongly. If the chamber is not purged properly, then a lower fluence at the output nozzle is obtained at the end of the processing chamber.

Table 5.2 shows that with distilled water flowing in the micro-channel, the insertion loss was reduced by 1.7 dB to 3.3 dB due to decreased refractive index contrast from the glass-water interface compared to the glass-air interface. The water filled the micro-channel by capillary effect.

The water diluted microsphere solution was used to fill the micro-channel. As indi-

vidual microsphere passed through the waveguide sensor, a signal drop of 0.13 dB to 0.14 dB was detected in red according to Figure 5.2. However, a static microsphere placed at the waveguide-micro-channel intersection produced a drop of ~2.4 dB in red according to Table 5.3. The discrepancy between the dynamic and static case was possibly due to the poor microsphere height-positioning relative to the waveguide in the dynamic case. When the microsphere was in a static position, it was likely that the microsphere was sitting in the V-groove at the bottom of the micro-channel and the full microsphere was blocking the waveguide. Hence, a high loss was detected due to absorbed, scattered and reflected light. When the microsphere was moving along the micro-channel, it was likely that the microsphere was floating in the water solution which did not fully intercept the optical path of the waveguide as much as in the static case. Hence, a much lower reduction in signal loss was detected.

In future work, engineering improvements are required for higher signal detection. A higher laser fluence for ablation to provide smoother and more vertical walls for deep channels (~30-40 μm) can potentially give a better result. Firstly, a lower insertion loss can be obtained due to reduction of the roughness of the channel walls. Secondly, a more vertical wall provides less reflection and deflection loss from the glass-water or glass-air interface. Thirdly, the V-groove formation at the bottom of the channel can potentially be eliminated offering a freer fluid-flow structure and better prediction of particle position relative to the waveguide. To address the problem encountered from detection of floating microspheres, waveguides closer to the surface with shallower micro-channels and covering the micro-channels should alleviate the problem and provide higher detection sensitivity. Shallower micro-channels with waveguides closer to the surface can intersect the floating spheres more efficiently due to similar vertical level of the waveguides and spheres. Covering the micro-channels can allow the microspheres to flow deeper in the micro-channels providing higher occultation of the light from the probing optical waveguides. These improvements should enhance the detection power.

Chapter 6

Significance of this Work

The fabrication of optical circuits, microfluidic structures and integrated bio-sensors has been demonstrated with various materials and microfabrication techniques. However, new methods and techniques are constantly being developed for improved efficiency in required applications. As mentioned in the "Background" section, laser direct fabrication of optical circuits and microcfluidic structures is a rapid and efficient way in the research environment for prototyping. So what has this project contributed to the scientific community? And what is the significance of this particular work on fabricating biophotonic lab-on-a-chip components and device?

6.1 Laser Welding

Laser welding has been in industry for decades. However, most attention has been directed toward the welding of metals. Glasses were limited to thermal bonding and application of adhesives which could change the properties (both mechanically and chemically) and produce toxic fumes. With the first demonstration of F_2-laser welding of glasses, the small niche of glass welding applications is expanded. Although this is a preliminary work in progress, the results show great potential in both the commercial and academic community. As previous glass-to-glass welding work done in using CO_2 [24, 25] and HF

chemical laser [32], the deep penetration method was employed in which the laser energy was absorbed to achieve bulk heating. This heating effect is not desirable since the high thermal stresses weaken the brittle glass materials and cause fractures. In contrast, F_2-laser welding showed no observable fractures of the glass afterwards. Moreover, no bulk heating was required to initiate the fusing process. Hence, no thermal stresses and chemical change were noticed in bulk samples.

Laser welding of glasses with F_2 laser can also offer another method of sealing glass lab-on-a-chip devices. PDMS, which is a type of polymer, has been used extensively for fabrication of microfluidic structures and sealing of these lab-on-a-chip devices. It can be used to seal the micro-channels reversibly, or irreversibly depending on the surface treatment applied. However, glasses and polymers are different materials which have different optical, mechanical and chemical properties. This posts undesirable effects including different thermal expansion coefficient causing shifting of materials one relative to the other, compensation of light propagation due to different refractive indices, different absorption and transmission spectrums, and restriction on the kind of solvents being used. With the F_2-laser, applications include micromachining with a feature size of approximately 100 nm, fused silica refractive index modification of larger than 10^{-3} and the recently demonstrated welding of glasses can all be utilized for biophotonic lab-on-a-chip fabrications. With the available capabilities, the undesirable differences in materials can be overcome by monolithic integration of optical circuits, microfluidic structures and sealing with fused silica. Further work needs to be done to identify the welding strength and the optimal welding formation.

6.2 Ge-doped FHD Silica Optical Circuits

Ge-doped FHD silica optical circuits has been directly fabricated with electron beam densification [59] and UV irradiation [103] at 248 nm. And with the demonstration

of 157 nm irradiation of NiCr contact mask for optical circuit fabrication, it provides another efficient and rapid process for prototyping. The electron beam patterned NiCr layer acts as the amplitude mask for defining the planar optical circuit structure. A positive refractive index modification of greater than $3.7\text{x}10^{-3}$ due to 157 nm exposure can be achieved which is comparable to the saturated index change value of $4\text{x}10^{-3}$ using KrF laser at 248 nm [103]. Although a saturation value for index change has not been determined for the case of 157 nm irradiation, it is apparent from the nonuniform irradiation that the index saturation has not been reached yet. This large index contrast can be used for writing of multi-mode optical circuits which is beneficial for specific applications. Hence, this is an attractive method for construction of both single and multi-mode planar optical circuit in addition to the complex structures the electron beam provides with a sub-micron resolution.

The direct-write technique defines the desirable buried photonic structures with a focused and shaped beam, whereas the bulk exposure method used for the FHD sample defines the light circuits according to the attached NiCr mask pattern. The latter case allows a parallel process in which the number of different components fabricated at once is restricted by the beam size. The drawback is the amount of work required to fabricate the attached contact mask which is a multi-step process involving harmful chemicals and extensive knowledge on their properties. On the other hand, the direct-write method does not require any chemicals and the patterns are defined by the computer controlled *xyz* stage. Also, it is able to write similar light guiding structures in parallel. Both of these techniques provide a rapid turnover time for iterations of the design cycle each involving designing, fabrication and testing of the device. Depending on the type of optical circuits needed, one method is more advantageous than the other.

The ability to form planar optical circuit with a combination of e-beam lithography, photolithography and UV irradiation is a fascinating topic on its own. However, with the addition of the F_2-laser micromachining ability, the applicable field of interest has

been broadened. As discussed in the previous section, this has a great potential in the fabrication of lab-on-a-chip devices with photonic capabilities. Especially when the near surface characteristics of the defined optical circuits can be used as an advantage in which only shallow microfluidics are required comparing to the ones needed for buried optical circuits. As seen in the results section, the micro-channels have vertical walls at the shallow section and begin to taper off into a V-groove as the ablation go deeper. This has an undesirable effect on particle flow because of the potential particle arrest on the V-groove preventing continuous flow. Photolithography plus wet chemical/RIE etching offer high aspect ratio micro-channels in glass. However, the process requires multiple steps and chemicals in addition to the slow etch rate. There are obviously advantages and disadvantages for various methods, but the merits of each can sometimes overcome the negatives and a compromise is reached for an overall optimal result.

To provide a glimpse in what this platform can offer, Ruano et al. [7, 8] has proven the usefulness of a similar structure on a FHD silica-on-silicon platform by performing fluorescence measurement with a micro-chamber fabricated by RIE. The etching was a slow process having an etch rate of 294 nm/min. In comparison to the F_2 laser, it provides a higher etch rate although the depth is limited for vertical walls. In future work, it can be shown that a similar device can be constructed with similar performance and faster fabrication time.

6.3 Monolithic Integration of Waveguides and Micro-channels

Monolithic integration of optical circuits, micro-channels and micro-analysis chambers is important in bio-sensing application. Several previous demonstrations have proved the performance in these single chip devices. Applications including fluorescence [7, 8, 97–99] and absorption [96, 100] measurement, and cytometer [100] have shown their

promises in the research laboratories. However, Rapid prototyping is not feasible due to the significant amount of fabrication steps involved. With F_2-laser, complex structured buried waveguides and micro-channels are easily implemented into bulk fused silica with the appropriate amplitude mask. The design is programmed into a computer which controls the *xyz* stage holding the sample and the laser repetition rate. Together, single-step integration of waveguides and micro-channels is possible without the need of chemicals or multi-step lithography techniques.

Although direct laser integration of refractive index structures with microfluidics offers a power tool for custom designed biophotonics lab-on-a-chip fabrication, it is not suitable for high-volume production. Laser direct fabrication is able to produce custom lab-on-a-chip structures one design at a time. However, conventional semiconductor microfabrication techniques can provide a parallel process with lithography and wet etching. Fixed design has to be used without the flexibility of alternating the structure as desired unless a new mask is fabricated. This involves additional cost and is time consuming for each new iteration of a new design. Hence, different methods have their own merits and drawbacks. Clearly, F_2-laser direct fabrication is suited for the purpose of biochip designing and prototyping for low volume production.

The purpose of this device was to demonstrate the single-step monolithic integration of micro-channels and optical waveguides. This device can be applied to a wide range of wavelengths for bio-sensing application from UV to infrared due to the inherent properties of UV-grade fused silica glass. The flow cytometry tested on a biochip by Friis et al. [100] contains a circular flow chamber with six waveguides positioned radially around. One waveguide is used for guiding excitation light and the other five waveguides are used for collecting scattered excitation and emitted fluorescent light from the bio-sample. Comparing to the lab-on-a-chip arrangement with a waveguide intersecting a micro-channel orthogonally, Friis et al.'s [100] more complex arrangement should provide a better detection sensitivity because of the extra waveguides for collecting scattered

light in addition to the waveguide opposite the excitation waveguide for collecting the forward scatter light. Although no definite measurement values were present by Friis et al., it is believed by them that its results using fluorescent stained polymer beads provided reasonable performance. With the current configuration, the detection scheme is based on the absorption and scattered light loss while the polystyrene microspheres pass through the optical waveguide sensor. In future work, a more complex optical circuits combined with microfluidic structures will be fabricated for both fluorescence and absorption applications by simply altering the design via the computer program.

Recent interest in biochips for analyzing bio-materials require UV to visible wavelengths due to the intrinsic absorption near that spectrum of light. Ge-doped silica waveguide is a popular optical guiding structure in the telecommunication industry and in fabrication of biochip. However, there are absorption centers preventing optical guiding of wavelength below 400 nm [96]. Mogensen et al. fabricated the refractive index structures with silicon oxynitride by plasma-enhanced chemical-vapor deposition with RIE etching for UV optical guiding with micro-channels by RIE etching. The multi-step process involves chemicals and is time consuming. With F_2-laser single-step integration in bulk UV-grade fused silica, it provides a potential biochip platform for analyzing various biological and chemical materials with wavelengths ranging from UV to infrared. The F_2 buried waveguides are demonstrated to be able to guide light from visible (635 nm) to Infrared (1550 nm). Further, the optical property of UV-grade fused silica offers a high transmission of >80% from ~190 nm to ~2000 nm which indicates a promising material for UV optical guiding.

Optical waveguides in the biophotonics lab-on-a-chip should be low in propagation loss ideally. The propagation loss for various biochips range from 0.5 dB/cm to 6.2 dB/cm [96–98]. The shallow F_2 buried waveguides have an estimated propagation loss which ranges from 3.6 dB/cm to 13.5 dB/cm. A lower propagation loss provides higher optical probing power for analyzing the sample in the microfluidic structure or micro-analysis

chamber. There is a tradeoff which comes back to the different techniques in fabrication process. Again, the most important achievement in direct F_2 laser direct writing of waveguide is the absence of the lithography, RIE etching, or cladding layer deposition steps. The higher propagation loss can be compensated by lowering the coupling loss and increasing the input excitation source.

Further, the current device employs the capillary effect for the flowing of microspheres in the microfluidic channel. A more controlled pumping mechanism for the fluid flow is more desirable. Capillary electrophoresis is used widely for separation and transportation of fluids and materials in micro-channels especially for biophotonic lab-on-a-chip devices [96–99]. An electrically regulated electrophoresis offers controllability on the flow rate and direction, and separation and sorting of different bio-materials. This issue will be addressed in future work where electrodes will be positioned at appropriate sample reservoirs with properly applied voltages.

Although the device demonstration showed limited function, the large margin for improvement indicates the countless number of applications this simple device is able to offer. The ability to write buried refractive index modification with Δn of $\sim 10^{-3}$ in glass and to etch high aspect-ratio microfluidic channels with smooth walls using the F_2-laser system open up the possibility of rapid integration of complex structured biophotonics lab-on-a-chip. This lays the groundwork for direct laser microfabrication of biochips and provides insight into the capabilities lab-on-a-chip offer when photonic components are combined with microfluidic system.

Chapter 7

Conclusions

Direct F_2 laser micromachining has proven to be an alternative fabrication technique for biophotonic lab-on-a-chip components and microfluidic channel integrated with optical waveguide. UV grade fused silica and Ge-doped FHD silica-on-silicon were used due to their material properties: hard, durable, resistant to most acids and solvents, and low thermal expansion. They are also optically transparent from visible to infrared and these photosensitive glasses offer a suitable platform for formation of optical waveguides. Survey experiment on F_2-laser micro-welding of fused silica coverslip with glass optical fiber was conducted. Micromachining of micro-channel intersecting an optical waveguide in bulk fused silica was demonstrated as a particle detector.

F_2-laser welding of fused silica coverslip and glass optical fiber was demonstrated. A narrow single-pulse fluence range of 2.61 J/cm^2 to 3.66 J/cm^2 for a focal spot size of 25 μm x 25 μm provided the transmission welding through the $\sim$160 μm fused silica coverslip with the fiber. The contact weld points fused $\sim$4% of the fiber circumference with an average molten glass reflow height of $\sim$1.3 to 1.4 μm. It is believed that the molten glass was ejected from the fused silica coverslip and mixed with the molten glass on the optical fiber. The molten glass resolidified and formed contact weld points which wrapped around the fiber. This survey experiment provides an insight into the potential

laser-fusing of transparent glasses.

Ge-doped FHD silica optical circuits were fabricated containing Ge-doped concentration of 3%, 7%, and 10% with F_2-laser exposure. Straight waveguides in each Ge-doped concentration with a width of 4 μm and depth of 2 μm were tested. Only the waveguide samples with a Ge content of 3% and 7% with a net fluence of 65.3 J/cm^2 and 33.6 J/cm^2 were able to guide 632.8 nm light. Evidence of refractive index modification was observed under a DIC microscope. Further, Y-branches (Ge-doped content of 3%) fabricated with a net fluence of 68.9 J/cm^2 give rise to multi-mode guiding in 632.8 nm light. This provided an estimated refractive index change of $3.7\text{x}10^{-3}$ for a 2 μm wide and deep waveguide using a 2-D Optiwave BPM software.

F_2-laser formed waveguides in fused silica with depths of 10 μm to 25 μm, width of 6 μm, and length of 0.5 mm were fabricated with a net fluence of 20 kJ/cm^2. The transverse modal width ($\frac{1}{e^2}$ for the waveguides ranged from 10.3 μm to 15.2 μm in red (635 nm) and 15.4 μm to 16.8 μm in IR (1550 nm). The refractive index changes for the fabricated waveguides were estimated using the RSoft software and ranged from $5.5\text{x}10^{-4}$ to $8.2\text{x}10^{-4}$ in red and $3.1\text{x}10^{-3}$ to $3.3\text{x}10^{-3}$ in infrared. The insertion loss ranges from $\sim$12 dB to 19 dB. The measured propagation loss for waveguide depths of 10 μm to 20 μm ranged from 3.6 dB/cm to 13.5 dB/cm.

The waveguide depth of 10 μm was chosen for the fabrication of the device with a intersecting channel. The micro-channel is 30 μm wide and 35 μm deep with a wall angle of $\sim 11^{\circ}$. The high fluence of $\sim$4 J/cm^2 was available for micro-channel fabrication to obtain smooth and steep walls. Polystyrene microspheres were flowed pass the waveguide probe and were detected by observing a transmission power drop at the waveguide output. In the dynamic case where the microsphere flowed pass the waveguide, a signal drop of $\sim$0.13 to 0.14 dB was detected. In the static case where the microsphere remained stationary at the waveguide probe, a $\sim$20 fold increase in signal drop of $\sim$2.4 dB was detected. This demonstrated the applicability of the device as a cytometer.

F_2 laser system is demonstrated to be an alternative method for rapid prototyping of biophotonic lab-on-a-chip components and device. Combining F_2-laser abilities to micromachine micro-channels and to form optical circuits in photosensitive glasses allow flexible fabrication of biophotonic lab-on-a-chip structures. The significance of incorporating an optical waveguide into a micro-fluidic platform is the added optical capability to analyze sample content. The demonstration and analysis of this simple cytometry device in bulk fused silica offers insight into the capabilities and potential applications for laser fabricated glass biophotonic lab-on-a-chip devices. Moreover, the groundwork is laid for rapid laser prototyping of custom-designed microfluidic biochips interlaced with integrated-optical circuits to define a new generation of highly functional bio-sensor and lab-on-a-chip devices.

Bibliography

[1] S. C. Terry, J. H. Jermann, and J. B. Angell, "A gas chromatographic air analyzer fabricated on silicon wafer," *IEEE Trans. Electron. Devices*, vol. ED-26, pp. 1880–1886, 1979.

[2] A. Manz, N. Graber, and H. M. Widmer, "Miniaturized total chemical analysis systems: a novel concept for chemical sensing," *Sensors and Actuators*, vol. B1, pp. 244–248, 1990.

[3] C. S. Effenhauser, A. Manz, and H. M. Widmer, "Glass chips for high-speed capillary electrophoresis," *Ana. Chem.*, vol. 65, pp. 2637–2642, 1993.

[4] Z. H. Fan and D. J. Harrison, "Micromachining of capillary electrophoresis injectors and separators on glass chips and evaluation of flow at capillary intersections," *Anal. Chem.*, vol. 66, pp. 177–184, 1994.

[5] S. C. Jacobson, R. Hergenroder, L. B. Koutny, and J. M. Rarnsey, "Open channel electrochromatography on a microchip," *Anal. Chem.*, vol. 66, pp. 2369–2373, 1994.

[6] A. Daridon, V. Fascio, J. Lichtenberg, R. Wutrich, H. Langen, E. Verpoorte, and N. F. de Rooij, "Multi-layer microfluidic glass chips for microanalytical applications," *Fresenius J. Anal. Chem.*, vol. 371, pp. 261–269, 2001.

[7] J. M. Ruano, D. Ortega, J. R. Bonar, A. J. McLaughlin, M. G. Jubber, J. M. Cooper, and J. S. Aitchison, "Fabrication of integrated microanalytical chambers

and channels for biological assays using flame hydrolysis deposition glass," *Microelec. Eng.*, vol. 46, pp. 419–422, 1999.

[8] J. M. Ruano, V. Benoit, J. S. Aitchison, and J. M. Cooper, "Flame hydrolysis deposition of glass on silicon for the integration of optical and microfluidic devices," *Anal. Chem.*, vol. 72, pp. 1093–1097, 2000.

[9] L. A. Tse, P. J. Hesketh, D. W. Rosen, and J. L. Gole, "Stereolithography on silicon for microfuidics and microsensor packaging," *Microsyst. Technol.*, vol. 9, pp. 319–323, 2003.

[10] A. Han, O. Wang, S. K. Mohanty, M. Graff, and B. Frazier, "A multi-layer plastic packaging technology for miniaturized bio analysis systems containing integrated electrical and mechanical functionality," *Proceedings of the Second Annual International IEEE-EMB Special Topic Conference on Microtechnologies in Medicine and Biology*, 2002.

[11] M. A. Roberts, J. S. Rossier, P. Bercier, and H. Girault, "UV laser machined polymer substrates for the development of microdiagnostic systems," *Anal. Chem.*, vol. 69, pp. 2035–2042, 1997.

[12] J. C. McDonald, D. C. Duffy, J. R. Anderson, D. T. Chiu, H. Wu, J. A. Schueller, and G. M. Whiteside, "Fabrication of microfluidic systems in poly(dimethylsiloxane)," *Electrophersis*, vol. 21, pp. 27–40, 2000.

[13] Y. P. Li and C. H. Henry, "Silica-based optical integrated circuits," *IEE Proc. Optoelectronics*, vol. 143(5), pp. 263–280, 1996.

[14] T. H. Maiman, "Stimulated optical radiation in ruby," *Nature*, vol. 187, pp. 493–494, 1960.

[15] P. R. Herman, B. Chen, D. J. Moore, and M. C. Retnam, "Photoablation studies of polymers, quartz, and semiconductors with vacuum ultraviolet laser radiation," *Mat. Res. Soc. Symp. Proc.*, vol. 236, pp. 53–58, 1992.

[16] P. R. Herman, K. Beckely, B. Jackson, K. Kurosawa, D. Moore, T. Yamanishi, and J. Yang, "Processing applications with the 157-nm fluorine excimer laser," *Proc. of the SPIE*, vol. 2992, pp. 86–95, 1997.

[17] P. R. Herman, R. S. Marjoribanks, A. Oettl, K. Chen, I. Konovalov, and S. Ness, "Laser shaping of photonic materials: deep-ultraviolet and ultrafast lasers," *Appl. Surf. Sci.*, vol. 154-155, pp. 577–586, 2000.

[18] K. Sugioka, K. Obata, K. Midorikawa, M. H. Hong, D. J. Wu, L. L. Wong, Y. F. Lu, and T. C. Chong, "Advanced materials processing based on interaction of laser beam and a medium," *J. Photochem. Photobio. A*, vol. 158, pp. 171–178, 2003.

[19] C. Korner, R. Mayerhofer, M. Hartmann, and H. W. Bergmann, "Physical and material aspects in using visible laser pulses of nanosecond duration for ablation," *Appl. Phys. A*, vol. 63, pp. 123–131, 1996.

[20] T. Funayama, H. Suzuki, H. Arakane, H. Shibutani, and O. Horiuchi, "Micro-welding of glass substrate by YAG laser. I. proposal of a new welding method using YAG laser and it's feasibility study," *Journal of the Japan Society of Precision Engineering*, vol. 68(9), pp. 1231–1235, 2002.

[21] C. Luo and L. Lin, "The application of nanosecond-pulsed laser welding technology in MEMS packaging with a shadow mask," *Sensors and Actuators A (Physical)*, vol. A97-98, pp. 398–404, 2002.

[22] S. Kaufmann, A. Otto, and G. Luz, "Laser beam joining of optical fibers in silicon V-grooves," *Proceedings of the SPIE - The International Society for Optical Engineering*, vol. 3933, pp. 371–8, 2000.

[23] M. J. Wild, A. Gillner, and R. Poprawe, "Advances in silicon to glass bonding with laser," *Proceedings of the SPIE - The International Society for Optical Engineering*, vol. 4407, pp. 135–41, 2001.

[24] E. K. Phitzer and R. Turner, "Quartz working with CO_2 laser," *J. Sci. Instruments Series 2*, vol. 1, p. 360, 1968.

[25] C. Deminet, "CO_2 laser welding of glass," *Laser Materials Processing ICALEO '87*, pp. 241–245, 1987.

[26] R. Witte, H. Herfurth, and S. Heinemann, "Laser joining of glass with silicon," *Proceedings of the SPIE - The International Society for Optical Engineering*, vol. 4637, pp. 487–495, 2002.

[27] W. Lee, F. Huang, and J. S. Shie, "Wafer bonding by low-temperature soldering," *Sens. Actuators A.*, vol. 85, pp. 330–334, 2000.

[28] F. Niklaus, P. Enoksson, P. Griss, E. Kalvesten, and G. Stemme, "Low-temperature wafer-level transfer bonding," *J. Microelectromech. Syst.*, vol. 10, pp. 525–531, 2001.

[29] H. Henmi, S. Shoji, Y. Shoji, K. Yoshimi, and M. Esashi, "Vacuum packaging for microsensors by glass-silicon anodic bonding," *Sens. Actuators A.*, vol. 43, pp. 243–248, 1994.

[30] T. Rogers and J. Kowal, "Selection of glass, anodic bonding conditions and material compatibility for silicon-glass capacitive sensors," *Sens. Actuators A.*, vol. 46-47, pp. 113–120, 1995.

[31] A. Saran, D. C. Abeysinghe, R. Flenniken, and J. T. Boyd, "Anodic bonding of optical fibers-to-silicon for integrating mems devices and opticla fibers," *J. Micromech. Microeng.*, vol. 13, pp. 346–351, 2003.

[32] R. C. Joeckle and A. Sontag, "Deep-penetration welding of glass by HF laser," *Proceedings of the International Conference on Lasers '85*, pp. 553–6, 1986.

[33] V. Kagan and R. G. Bray, "Advantages and limitations of laser welding technology for semi-crystalline reinforced plastics," *Honeywell Laboratories*, 2000.

[34] K. O. Hill, Y. Fujii, D. C. Johnson, and B. S. Kawasaki, "Photosensitivity in optical fiber waveguides: Application to reflection filter fabrication," *Appl. Phys. Lett.*, vol. 32, no. 10, pp. 647–649, 1978.

[35] G. Meltz, W. W. Morey, and W. H. Glenn, "Formation of Bragg gratings in optical fibers by a transverse holographic method," *Optics Letters*, vol. 14, no. 15, pp. 823–825, 1989.

[36] J. Albert, B. Malo, F. Bilodeau, D. C. Johnson, K. O. Hill, Y. Hibino, and M. Kawachi, "Photosensitivity in Ge-doped silica optical waveguides and fibers with 193-nm light from an ArF excimer laser," *Optics Letters*, vol. 19, no. 6, pp. 387–389, 1994.

[37] P. E. Dyer, R. J. Farley, R. Giedl, K. C. Byron, and D. Reid, "High reflectivity fibre gratings produced by incubated damage using a 193nm ArF laser," *Elec. Letters*, vol. 30, no. 11, pp. 860–862, 1994.

[38] K. P. Chen and P. R. Herman, "Photosensitization of standard fibers with deep UV laser radiation," *J. Lightwave Tech.*, vol. 21, no. 9, pp. 1958–1968, 2003.

[39] A. Othonos, "Fiber Bragg gratings," *Rev. Sci. Instrum.*, vol. 68, no. 12, pp. 4309–4341, 1997.

[40] D. P. Hand and P. S. J. Russell, "Photoinduced refractive-index changes in germanosilicate fibers," *Optics Letters*, vol. 15, no. 2, pp. 102–104, 1990.

[41] M. G. Sceats, G. R. Atkins, and S. B. Poole, "Photolytic index changes in optical fibers," *Annu. Rev. Mater. Sci.*, vol. 23, pp. 381–410, 1993.

[42] D. L. Williams, S. T. Davey, R. Kashyap, J. R. Armitage, and B. J. Ainslie, "Direct observation of UV induced bleaching of 240nm absorption band in photosensitive germanosilicate glass fibers," *Elec. Letters*, vol. 28, no. 4, pp. 369–371, 1992.

[43] L. Dong, J. L. Archambault, L. Reekie, P. S. J. Russell, and D. N. Payne, "Photoinduced absorption change in germanosilicate preforms: evidence for the color-center model of photosensitivity," *Applied Optics*, vol. 34, no. 18, pp. 3436–3440, 1995.

[44] D. C. Allan, C. Smith, N. F. Borrelli, and T. P. Seward III, "193-nm excimer-laser-induced densification of fused silica," *Optics Letters*, vol. 21, no. 24, pp. 1960–1962, 1996.

[45] N. F. Borrelli, C. Smith, D. C. Allan, and T. P. Seward III, "Densification of fused silica under 193-nm excitation," *J. Opt. Soc. Am. B*, vol. 14, no. 7, pp. 1606–1615, 1997.

[46] R. E. Schenker and W. G. Oldham, "Ultraviolet-induced densification in fused silica," *J. Appl. Phys.*, vol. 82, pp. 1065–1071, 1997.

[47] N. F. Borrelli, C. M. Smith, and D. C. Allan, "Excimer-laser-induced densification in binary silica glasses," *Optics Letters*, vol. 24, no. 20, pp. 1401–1403, 1999.

[48] F. Piao, W. G. Oldham, and E. E. Haller, "Ultraviolet-induced densification of fused silica," *J. Appl. Phys.*, vol. 87, no. 7, pp. 3287–3293, 2000.

[49] X. M. Wei, K. P. Chen, D. Coric, P. R. Herman, and J. Li, "F_2-laser microfabrication of buried waveguide structures in transparent glasses," *Proc. SPIE*, vol. 4637, pp. 251–257, 2002.

[50] E. J. Friebele and P. L. Higby, *Laser Induced Damage in Optical Materials.* NIST Spec. Pub., 1988.

[51] K. M. Davis, K. Miura, N. Sugimoto, and K. Hirao, "Writing waveguides in glass with a femtosecond laser," *Opt. Lett.*, vol. 21, pp. 1729–1731, 1996.

[52] D. Homoelle, S. Wielandy, A. L. Gaeta, N. F. Borrelli, and C. Smith, "Infrared photosensitivity in silica glasses exposed to femtosecond laser pulses," *Opt. Lett.*, vol. 24, pp. 1311–1313, 1999.

[53] D. Du, X. Liu, G. Korn, J. Squier, and G. Mourou, "Laser-induced breakdown by impact ionization in SiO_2 with pulse widths from 7ns to 150fs," *Appl. Phys. Lett.*, vol. 64, no. 23, pp. 3071–3073, 1994.

[54] B. C. Stuart, M. D. Feit, A. M. Rubenchik, B. W. Shore, and M. D. Perry, "Laser-induced damage in dielectrics with nanosecond to subpicosecond pulses," *Physical Review Letters*, vol. 74, no. 12, pp. 2248–2252, 1995.

[55] E. N. Glezer and E. Mazur, "Ultrafast-laser micro-explosions in transparent materials," *Appl. Phys. Lett.*, vol. 71, no. 7, pp. 882–884, 1997.

[56] T. E. Murphy, J. T. Hastings, and H. I. Smith, "Fabrication and characterization of narrow-band Bragg-reflection filters in silicon-on-insulator ridge waveguides," *J. Lightwave Tech.*, vol. 19, no. 12, pp. 1938–1942, 2001.

[57] R. J. Deri and E. Kapon, "Low-loss III-V semiconductor optical waveguides," *IEEE J. Quantum Elec.*, vol. 27, no. 3, pp. 626–640, 1991.

[58] T. L. Koch and U. Koren, "Semiconductor photonic integrated circuits," *IEEE J. Quantum Elec.*, vol. 27, no. 3, pp. 641–653, 1991.

[59] S. G. Blanco, A. Glidle, J. H. Davies, J. S. Aitchison, and J. M. Cooper, "Electron-beam-induced densification of Ge-doped flame hydrolysis silica for waveguide fabrication," *Appl. Phys. Lett.*, vol. 79, no. 18, pp. 2889–2891, 2001.

[60] G. C. Righini and S. Pelli, "Ion exchange in glass: A mature technology for photonic devices," *Proc. of the SPIE*, vol. 4453, pp. 93–99, 2001.

[61] M. Svalgaard, C. V. Poulsen, A. Bjarklev, and O. Poulse, "Direct UV writing of buried singlemode channel waveguides in Ge-doped silica films," *Elec. Letters*, vol. 30, no. 17, pp. 1401–1403, 1994.

[62] M. Svalgaard, "Direct writing of planar waveguide power splitters and directional couplers using a focussed ultraviolet laser beam," *Elec. Letters*, vol. 33, no. 20, pp. 1694–1695, 1997.

[63] M. Rothschild, D. J. Ehrlich, and D. C. Shave, "Effects of excimer laser irradiation on the transmission, index of refraction, and density of ultraviolet grade fused silica," *Appl. Phys. Lett.*, vol. 55, no. 13, pp. 1276–1278, 1989.

[64] J. Zhang, P. R. Herman, C. Lauer, K. P. Chen, and M. Wei, "157-nm laser-induced modification of fused-silica glasses," *Proc. of SPIE*, vol. 4274, pp. 125–132, 2001.

[65] C. Valdivia, X. M. Wei, D. Coric, and P. R. Herman, "F_2 laser-induced visible and infrared-confining buried waveguides in fused silica," *Conf. on Lasers and Electro-Optics Baltimore: Optical Society of America*, 2003.

[66] K. P. Chen, P. R. Herman, and R. Taylor, "Photosensitivity and application with 157-nm F_2 laser radiation in planar lightwave circuits," *J. Lightwave tech.*, vol. 21, no. 1, pp. 140–148, 2003.

[67] H. T. G. van Lintel, F. C. M. van de Pol, and S. Bouwstra, "A piezoelectric micropump based on micromachining of silicon," *Sens. Actuators*, vol. 15, pp. 153–167, 1988.

[68] M. Esashi, S. Shoji, and A. Nakano, "Normally closed microvalve and micropump fabricated on a silicon wafer," *Sens. Actuators*, vol. 20, pp. 163–169, 1989.

[69] S. Shoji, S. Nakagawa, and M. Esashi, "Micropump and sample-injector for integrated chemical analyzing systems," *Sens. Actuators A*, vol. 21, pp. 189–192, 1990.

[70] J. G. Smits, "Piezoelectric micropump with three valves working peristaltically," *Sens. Actuators A*, vol. 21, pp. 203–206, 1990.

[71] S. Shoji, M. Esashi, and T. Matsuo, "Prototype miniature blood gas analyser fabricated on a silicon wafer," *Sens. Actuators*, vol. 14, pp. 101–107, 1988.

[72] M. Esashi, "Integrated micro flow control systems," *Sens. Actuators A*, vol. 21, pp. 161–167, 1990.

[73] A. Manz, Y. Miyahara, J. Miura, Y. Watanabe, H. Miyagi, and K. Sato, "Design of an open-tubular column liquid chromatograpy using silicon chip technology," *Sens. Actuators B*, vol. 1, pp. 249–255, 1990.

[74] P. V. Zant, *Microchip Fabrication: A Practical Guide to Semiconductor Processing.* McGraw-Hill, 3 ed., 1997.

[75] S. Nonogaki, T. Ueno, and T. Ito, *Microlithography Fundamentals in Semiconductor Devices and Fabrication Technology.* Marcel Dekker, Inc., 1 ed., 1998.

[76] E. Kim, Y. N. Xia, and G. M. Whitesides, "Polymer microstructures formed by moulding in capillaries," *Nature*, vol. 376, pp. 581–584, 1995.

[77] L. Martynova, L. Locascio, M. Gaitan, G. Kramer, R. Christensen, and W. MacCrehan, "Fabrication of plastic microfluid channels by imprinting methods," *Anal. Chem.*, vol. 69, pp. 4783–4789, 1997.

[78] B. A. Grzybowski, R. Haag, N. Bowden, and G. M. Whitesides, "Generation of micrometer-sized patterns for microanalytical applications using a laser direct-write method and microcontact printing,"

[79] B. H. Jo, L. M. Van Lerberghe, K. M. Motsegood, and D. Beebe, "Three-dimensional micro-channel fabrication in polydimethylsiloxane (PDMS) elastomer," *J. Microelectromech. Syst.*, vol. 9, pp. 76–81, 2000.

[80] D. C. Duffy, O. J. A. Schueller, S. T. Brittain, and G. Whitesides, "Rapid prototyping of microfluidic switches in poly(dimethyl siloxane) and their actuation by electro-osmotic flow," *J. Micromech. Microeng.*, vol. 9, pp. 211–217, 1999.

[81] D. J. Beebe, J. S. Moore, Q. Yu, R. H. Liu, M. L. Kraft, B. H. Jo, and C. Devadoss, "Microfluidic tectonics: A comprehensive construction platform for microfluidic systems," *PNAS*, vol. 97, no. 25, pp. 13488–13493, 2000.

[82] A. Bertsch, S. Heimgartner, P. Cousseau, and P. Renaud, "Static micromixers based on large-scale industrial mixer geometry," *Lab on a Chip*, vol. 1, pp. 56–60, 2001.

[83] P. R. Herman, A. Yick, J. Li, N. Munce, L. Lilge, E. Jervis, and S. Krylov, "F_2-laser micromachining of microfluidic channels and vias for biophotonic chip applications," *Conf. on Lasers and Electro-Optics Tech. Digest (OSA, Wash DC, 2003) Baltimore*, vol. CFL5, pp. 1–3, 2003.

[84] F. Wagner and P. Hoffmann, "Structure formation in excimer laser ablation of stretched poly(ethylene therephthalate) (PET): the influence of scanning ablation," *Appl. Phys A*, vol. 69, pp. S841–S844, 1999.

[85] Y. N. Shi, P. C. Simpson, J. R. Scherer, D. Wexler, C. Skibola, M. T. Smith, and R. A. Mathies, "Radial capillary array electrophoresis microplate and scanner for high-performance nucleic acid analysis," *Anal. Chem.*, vol. 71, pp. 5354–5361, 1999.

[86] M. Ueda, Y. Kiba, H. Abe, A. Arai, H. Nakanishi, and Y. Baba, "Fast separation of oligonucleotide and triplet repeat DNA on a microfabricated capillary electrophoresis device and capillary electrophoresis," *Electrophoresis*, vol. 21, pp. 176–180, 2000.

[87] S. Liu, Y. Shi, W. W. Ja, and R. A. Mathies, "Optimization of high-speed DNA sequencing on microfabricated capillary electrophoresis channels," *Anal. Chem.*, vol. 71, pp. 566–573, 1999.

[88] B. M. Paegel, C. A. Emrich, G. J. Wedemayer, J. R. Scherer, and R. A. Mathies, "High throughput DNA sequencing with a microfabricated 96-lane capillary array electrophoresis bioprocessor," *PNAS*, vol. 99, no. 2, pp. 574–579, 2002.

[89] P. Belgrader, S. Young, B. Yuan, M. Primeau, and L. A. Christel, "A battery-powered notebook thermal cycler for rapid multiplex real-time PCR analysis," *Anal. Chem.*, vol. 73, pp. 286–289, 2001.

[90] L. C. Waters, S. C. Jacobson, N. Kroutchinina, J. Khandurina, R. S. Foote, and J. M. Ramsey, "Microchip device for cell lysis, multiplex PCR, amplification, and electrophoretic sizing," *Anal. Chem.*, vol. 70, pp. 158–162, 1998.

[91] J. Khandurina, T. E. McKnight, S. C. Jacobson, L. C. Waters, R. S. Foote, and J. M. Ramsey, "Integrated system for rapid PCR-based DNA analysis in microfluidic devices," *Anal. Chem.*, vol. 72, pp. 2995–3000, 2000.

[92] A. Y. Fu, C. Spence, A. Scherer, F. H. Arnold, and S. R. Quake, "A microfabricated fluorescence-activated cell sorter," *Nat. Biotechnol.*, vol. 17, pp. 1109–1111, 1999.

[93] F. Arai, A. Ichikawa, M. Ogawa, T. Fukuda, K. Horio, and K. Itoigawa, "High-speed separation system of randomly suspended single living cells by laser trap and dielectrophoresis," *Electrophoresis*, vol. 22, pp. 283–288, 2001.

[94] G. Ocvirk, T. Tang, and D. J. Harrison, "Optimization of confocal epifluorescence microscopy for microchip-based miniaturized total analysis systems," *Analyst*, vol. 123, no. 7, pp. 1429–1434, 1998.

[95] G. Jiang, S. Attiya, G. Ocvirk, W. E. Lee, and D. J. Harrison, "Red diode laser induced fluorescence detection with a confocal microscope on a microchip for capillary electrophoresis," *Biosen. Bioelec.*, vol. 14, pp. 861–869, 2000.

[96] K. B. Mogensen, P. Friis, J. Hubner, N. Petersen, A. M. Jorgensen, P. Telleman, and J. P. Kutter, "Ultraviolet transparent silicon oxynitride waveguides for biochemical microsystems," *Optics Letters*, vol. 26, no. 10, pp. 716–718, 2001.

[97] J. Hubner, K. B. Mogensen, A. M. Jorgensen, P. Friis, P. Telleman, and J. P. Kutter, "Integrated optical measurement system for fluorescence spectroscopy in microfluidic channels," *Review of Sci. Instru.*, vol. 72, no. 1, pp. 229–233, 2001.

[98] K. B. Mogensen, J. El-Ali, A. Wolff, and J. P. Kutter, "Integration of polymer waveguides for optical detection in microfabricated chemical analysis systems," *Applied Optics*, vol. 42, no. 19, pp. 4072–4079, 2003.

[99] C. H. Lin, G. B. Lee, S. H. Chen, and G. L. Chang, "Micro capillary electrophoresis chips integrated with buried SU-8/SOG optical waveguides for bio-analytical application," *Sens. Actuators A*, vol. 107, pp. 125–131, 2003.

[100] P. Friis, K. Hoppe, O. Leistiko, K. B. Mogensen, J. Hubner, and J. P. Kutter, "Monolithic integration of microfluidic channels and optical waveguides in silica on silicon," *Applied Optics*, vol. 40, no. 34, pp. 6246–6251, 2001.

[101] L. Cui, T. Zhang, and H. Morgan, "Optical particle detection integrated in a dielectrophoretic lab-on-a-chip," *J. Micromech. Microeng.*, vol. 12, pp. 7–12, 2002.

[102] P. R. Herman, K. P. Chen, M. Wei, J. Zhang, J. Ihlemann, D. Schafer, G. Marowsky, P. Oesterlin, and B. Burghardt, "F_2-lasers: High-resolution optical processing system for shaping photonic components," *Laser Appl. in Microelectr. and Optoelectr. Manuf. SPIE Proc.*, vol. 4274, pp. 149–157, 2001.

[103] P. V. S. Marques, J. R. Bonar, A. M. P. Leite, and J. S. Aitchison, "Simultaneous UV direct writing of channel waveguides and bragg gratings in germanium-doped planar silica," *IEEE J. of Sel. Topics in Quan. Elec.*, vol. 8, pp. 1316–1322, 2002.

[104] A. Cleary, "Integration optical technologies for analytical sensing," Ph.D. thesis, University of Glasgow, 2003.

[105] I. A. Konovalov and P. R. Herman, "Ablation-induced stresses in fused silica by 157-nm F_2-laser irradiation," *Mat. Res. Soc. Symp.*, vol. 617, pp. J3.3.1–3.3.7, 2000.

[106] P. C. Hill, P. R. Herman, and R. Sia, "Spectral widths of a F_2 ($D'^3\prod_{2g} \rightarrow A'^3\prod_{2u}$) laser," *J. Appl. Phys.*, vol. 73, pp. 5274–5276, 1993.

[107] P. R. Herman, K. P. Chen, P. Corkum, A. Naumov, S. Ng, and J. Zhang, "Advanced lasers for photonic device microfabrication," *Riken Review*, vol. 32, pp. 31–35, 2001.

[108] P. R. Herman, K. P. Chen, P. Corkum, A. Naumov, S. Ng, and J. Zhang, "Advanced laser microfabrication of photonic components," *Proc. of SPIE*, vol. 4088, pp. 345–350, 2000.

[109] C. Valdivia, "Integration of self-assembled colloidal photonic crystals within laser-microfabricated optical circuits," M.A.Sc thesis, University of Toronto, 2003.